A Decentralized Approach for Modeling Organized Convection Based on Thermal Populations on Microgrids

R. A. J. Neggers[1] and P. J. Griewank[2]

[1]Institute for Geophysics and Meteorology, University of Cologne, Cologne, Germany, [2]Department of Meteorology and Geophysics, University of Vienna, Vienna, Austria

Abstract In this study, a spectral model for convective transport is coupled to a thermal population model on a two-dimensional horizontal "microgrid," covering the typical gridbox size of general circulation models. The goal is to explore new ways of representing impacts of spatial organization in cumulus cloud fields. The thermals are considered the smallest building block of convection, with thermal life cycle and movement represented through binomial functions. Thermals interact through two simple rules, reflecting pulsating growth and environmental deformation. Long-lived thermal clusters thus form on the microgrid, exhibiting scale growth and spacing that represent simple forms of spatial organization and memory. Size distributions of cluster number are diagnosed from the microgrid through an online clustering algorithm, and provided as input to a spectral multiplume eddy-diffusivity mass flux scheme. This yields a decentralized transport system, in that the thermal clusters acting as independent but interacting nodes that carry information about spatial structure. The main objectives of this study are (a) to seek proof of concept of this approach, and (b) to gain insight into impacts of spatial organization on convective transport. Single-column model experiments demonstrate satisfactory skill in reproducing two observed cases of continental shallow convection. Metrics expressing self-organization and spatial organization match well with large-eddy simulation results. We find that in this coupled system, spatial organization impacts convective transport primarily through the scale break in the size distribution of cluster number. The rooting of saturated plumes in the subcloud mixed layer plays a key role in this process.

Plain Language Summary Recent studies have emphasized the importance of the spatial structure of convective cloud fields in Earth's climate, yet this phenomenon is not yet represented well in Earth System Models (ESMs). This study explores a new way to achieve this goal, by considering spatial organization at the scale of small bubbles of rising air called thermals that together make up convective clouds. Populations of interacting thermals are modeled in a computationally efficient way on a small two-dimensional grid. This microgrid is then coupled to a convection scheme, which stands for the set of equations used to statistically represent the impact of convective transport at scales that remain unresolved in ESMs. The coupling makes the scheme decentralized, in that the transport becomes dependent on a population of longer-lived convective structures that slowly develop and evolve on the microgrid. The new scheme is tested for observed conditions at a meteorological site in the Southern Great Plains area of the United States, making use of a combination of high-resolution simulations and measurements to evaluate performance. Apart from proof of concept for the new modeling approach, the results provide new insights into how the spatial structure of convective cloud populations can affect its vertical transport.

1. Introduction

Recent studies have emphasized the important role played by the mesoscale organization of convective cloud populations in Earth's climate system (Wing et al., 2020). Marine cloud fields persistently cover large areas on the globe and often feature distinct forms of spatial organization (Stevens et al., 2020). As a result, the modulation in cloud mass by mesoscale organization can significantly affect the global energy and water budgets, and thus plays a role in cloud-climate feedback mechanisms (Vogel et al., 2016). Diurnal cycles of convection over land also feature organization in the mesoscale, involving distinct upscale growth (Neggers et al., 2019) and transitions between various convective modes (Gentine et al., 2013; Zhang & Klein, 2010). This has motivated intense research into convective organization, including various major field campaigns in recent years (Bony et al., 2017; Fast et al., 2019; Varble et al., 2021).

These reasons incentivize an accurate representation of impacts of mesoscale cloud organization in Earth System Models (ESMs) for weather prediction and climate simulation. However, achieving this has proven to be extremely difficult, contributing to the persistent problems with convective parameterization in general (Grabowski et al., 2006; Sherwood et al., 2014; Zhang et al., 2013). Convection schemes are typically formulated in only one dimension, the vertical (Arakawa, 2004). Accordingly, such schemes have access to information from a vertical column of gridboxes. Typical vertical discretizations of ESMs are within the range 10^1–10^2 m, which is fine enough to resolve the vertical structure of convective layers. In contrast, the horizontal plane is discretized much more coarsely, at 10^4–10^5 m. As a result, many forms of spatial mesoscale organization remain completely or at least partially unresolved. The mesoscale problem in essence thus comes down to a lack of horizontal resolution (Honnert et al., 2020).

With the "gray zone" problem ever shifting to smaller (boundary-layer) scales, a few recent studies have attempted to model the impact of unresolved thermal-scale fluctuations on the boundary layer, by adding perturbations in a stochastic way (Clark et al., 2021; Hirt et al., 2019; Kober & Craig, 2016). Other studies have taken a different route, exploring how horizontal resolution can somehow be added to subgrid-scale parameterizations. One idea is to give convection schemes access to information from neighboring columns, for example, by introducing cellular automata (Bengtsson et al., 2021). While this allows improved representation of mesoscale structures close to the filter scale and beyond, any forms of organization smaller than that are still not captured. Another idea that avoids this problem is to add a *microgrid* within each grid-cell, a concept referred to as *superparameterization* (Randall et al., 2003). These microgrids can be three dimensional (Jansson et al., 2019), but most commonly only two-dimensional microgrids are used, to keep things efficient. The 2D grid can be oriented in two ways; vertically or horizontally. Each orientation has its benefits; while the vertical (cross-sectional) grid resolves convective cells in a vertical plane and horizontal (lattice) grids can resolve phenomena such as spatial clustering in convective populations.

This study exclusively focuses on the horizontal microgrid approach. Various research models of this type have recently been proposed, differing considerably in configuration and formulation, for example, in their use of concepts from cellular automata (Ahmed & Neelin, 2019; Dorrestijn et al., 2013; Hottovy & Stechmann, 2015; Khouider et al., 2010). A key question that remains is how such models can best be configured to represent spatial clustering in cumulus cloud populations. This comes down to deciding on how to define the smallest building block of convection, of which the larger, long-lived coherent structures are made. A follow-up question is how to then connect the horizontal microgrid to vertical convective transport.

In this study, a two-step method is explored to address these questions. The first is to adopt the relatively short-lived *thermal* as the smallest building block of convection, a choice inspired by both classic studies on bubble theory (Scorer & Ludlam, 1953) and recent studies of thermals (Hernandez-Deckers & Sherwood, 2016; Morrison & Peters, 2018; Romps et al., 2021; Varble et al., 2014). An example of a thermal chain that makes up a surface-rooted shallow cumulus plume is shown in Figure 1. An object-based approach is adopted to model the evolution of such thermal clusters on a horizontal microgrid. To this purpose, the Binomials On Microgrids (BiOMi) population model (BiOMi, Neggers & Griewank, 2021) is used, which represents the life cycle and movement of convective thermals as Bernoulli processes. Thermal interaction takes place under rules that reflect observed physics in cumulus clouds. As a result, longer-lived coherent thermal clusters form that feature a gradual scale growth. Various recent studies have demonstrated that mesoscale self-organization is well captured by object-based population models of this kind (Böing, 2016; Haerter et al., 2019).

The second step is to couple the microgrid to a spectral transport model, which is the focus of this study. To this purpose, the Eddy-Diffusivity multiple Mass Flux scheme is used (ED(MF)^n, Neggers, 2015), which independently resolves individual segments of the discretized spectrum of transporting objects. Spectral schemes typically contain a closure for the number of objects as a function of size. This distribution is here sampled from the microgrid. This yields a bottom-up, *decentralized* closure technique, with the thermal clusters on the microgrid acting as independent but interacting nodes. Each node carries information about the spatial organization around it, and has memory of how this organization formed. This can act on time scales much longer than the life cycle of individual thermals. Through the coupling, BiOMi functions as a "plume generator" through which the evolving spatial organization on the microgrid can affect transport, by altering the number distribution of transporting objects in the simulated domain.

a) w [m s^{-1}]   b) q_l [g kg^{-1}]
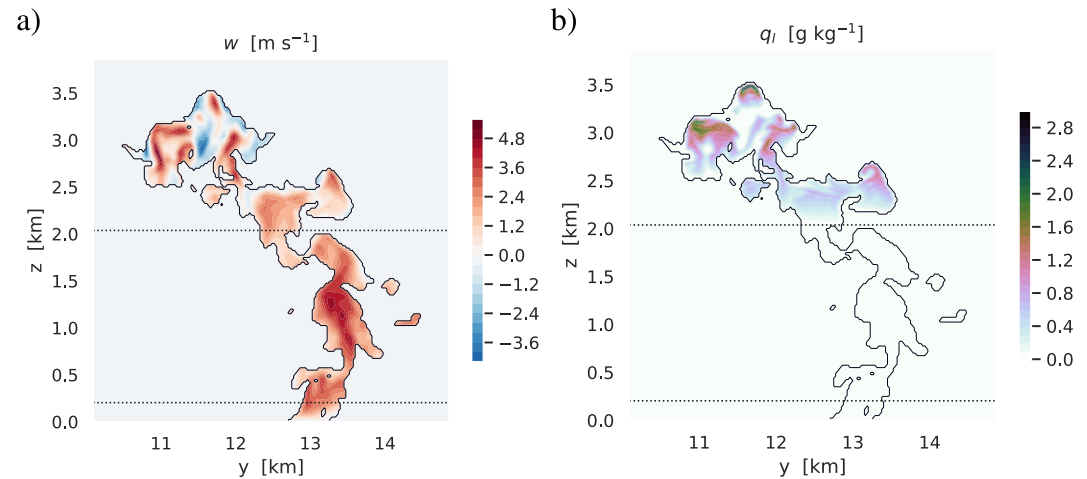
Figure 1. Vertical cross section through a surface-rooted convective plume as sampled from a LASSO LES of shallow cumulus observed on 11 June 2016 at the Atmospheric Radiation Measurement Southern Great Plains site. The simulation and cluster sampling are fully described by Griewank et al. (2021), as briefly summarized in Sections 3 and 4. Shown are (a) object vertical velocity w and (b) cloud liquid water q_l. The cluster outline is indicated by the solid black line. The two dotted lines indicate mixed-layer top ($z/h = 1$) and surface layer top ($z/h = 0.1$). The local maxima in w can be interpreted as thermal cores, forming a chain that makes up the plume.

The new framework, here named BiOMi-ED(MF)^n, is tested for two prototype diurnal cycles of continental shallow convection at the Southern Great Plains (SGP) site of the Atmospheric Radiation Measurement (ARM) program. The cases are selected from the LASSO library of shallow cumulus days (LES ARM Symbiotic Simulation and Observation activity, Gustafson et al., 2020). Both days feature simple forms of spatial organization (Neggers et al., 2019), but also show distinct differences in cloud height and depth. The framework is implemented in an LES code as a subgrid scheme and applied as a Single-Column Model (SCM). The model is evaluated against LASSO data sets, including both observational data and LES results. Apart from seeking proof of concept, our main goal is to use this system to better understand how spatial organization can affect shallow convective transport in continental boundary layers, and how this modulates the diurnal cycle.

The formulation of the coupled BiOMi-ED(MF)^n system is described in Section 2. The calibration of the framework is discussed in Section 3, while the simulated cumulus cases and the design of the SCM experiments are described in Section 4. Results are presented in Section 5 and are further interpreted in Section 6. A summary of the main conclusions and a brief outlook on future research are provided in Section 7.

2. Model Components

All model components have been proposed and described in previous studies, and for a detailed description we refer to the associated papers. Their characteristics essential for this study are briefly summarized below. Only new elements related to their coupling will be formulated and briefly discussed.

2.1. BiOMi

BiOMi is a discretely formulated object-based population model defined on a horizontal microgrid (Neggers & Griewank, 2021). While it has various potential applications, in this study it is used to model populations of relatively short-lived convective thermals. These thermals are born and live on the grid, and complete a life cycle while potentially moving around. These processes are modeled as Bernoulli trials, which implies a binomial nature in the population statistics. In addition, it makes the model computationally efficient, as the behavior of large numbers of thermals can be predicted using a single binomial sample.

The position of thermals on the grid is determined by both birth location and interaction with other thermals. This interaction happens under specified rules of transition, which in this application are defined to reflect the physics and internal dynamics of shallow cumulus cloud populations. Neggers and Griewank (2021), hereafter referred to

as NG21, showed that only two specific rules of interaction already led to clustering on the grid that mimics the spatial behavior of shallow cumulus cloud populations. For a full description of these rules, we refer to NG21, but the main equations required for understanding the results presented in this study are briefly summarized below.

At the foundation of BiOMi is the reference thermal birth rate $\dot{B}$ (adopting NG21 notation), or the number of new thermals born per unit area and unit time within a large reference domain. This domain is assumed large enough to fully sample a cumulus cloud population. Multiplying $\dot{B}$ with the domain area L^2 and time step Δt yields the total number of thermal births within the domain, $B = \dot{B}L^2\Delta t$. These births are then distributed over all microgrid cells within the reference domain, N in total. The probability that a single birth takes place within a specific cell is $p = 1/N$. Associated with this configuration is the binomial probability mass function F that depends on B and p,

$$\mathrm{F}(b, B, p) = \binom{B}{b} p^b (1 - p)^{(B-b)}. \tag{1}$$

with B and p given, randomly drawing one sample from this function in each microgrid cell per time step then yields a stochastic number of new thermals, b, to be added in the cell.

The two simple rules of thermal interaction described by NG21 both act on probability p, perturbing it locally. They are defined as follows:

- *Rule 1: Pulsating growth*: The birth probability of thermals increases from the background value p close to cells in which a number of thermals n are already present. This is achieved by defining the following perturbation p',

$$p' = C_f f_p n \tag{2}$$

where C_f is a constant of proportionality and f_p is a two-dimensional spatial impact field with radius r_f, for simplicity assumed to be cone shaped,

$$f_p = \begin{cases} 1 - r/r_f & \text{for } r < r_f \\ 0 & \text{for } r \geq r_f. \end{cases} \tag{3}$$

here, r is the distance to a grid cell of interest. In every cell on the microgrid, the perturbation field p' resulting from thermals present in all other cells is locally added to the spatially uniform reference probability p. This yields a new cumulative field p_c that can be spatially heterogeneous.

- *Rule 2: Environmental deformation*: The cumulative probability field p_c is uniformly scaled such that the large-scale averaged birth rate $\dot{B}$ is conserved, yielding a new probability field $\tilde{p}$,

$$\tilde{p} = \frac{1}{N} \frac{p_c}{\langle p_c \rangle}, \tag{4}$$

where the brackets indicate the average over the grid.

Implementation of these two rules is then achieved by using $\tilde{p}$ instead of p when sampling the binomial function Equation 1 for calculating the number of new thermals b born in each microgrid cell.

How rules 1 and 2 act in conjunction is schematically summarized in Figure 3. Rule 1 creates locally strong positive perturbations in the $\tilde{p}$ field near existing thermal clusters, while Rule 2 ensures that on average the reference birth rate $\dot{B}$ remains constrained by external forcings. In effect, Rule 2 thus acts to enforce this global constraint, by further suppressing the thermal birth rate in areas already void of thermals. In nature, this can happen through compensating subsidence and adiabatic heating by gravity waves induced by cumulus clouds (Bretherton & Smolarkiewicz, 1989), or mesoscale circulations induced by radiative cooling (Bretherton et al., 2005; Muller & Held, 2012). Figure 1 shows an example of thermal clustering as observed in an LES of shallow cumulus, featuring a chain of convective thermals that together make up a surface-rooted plume. At 2 km height it reaches
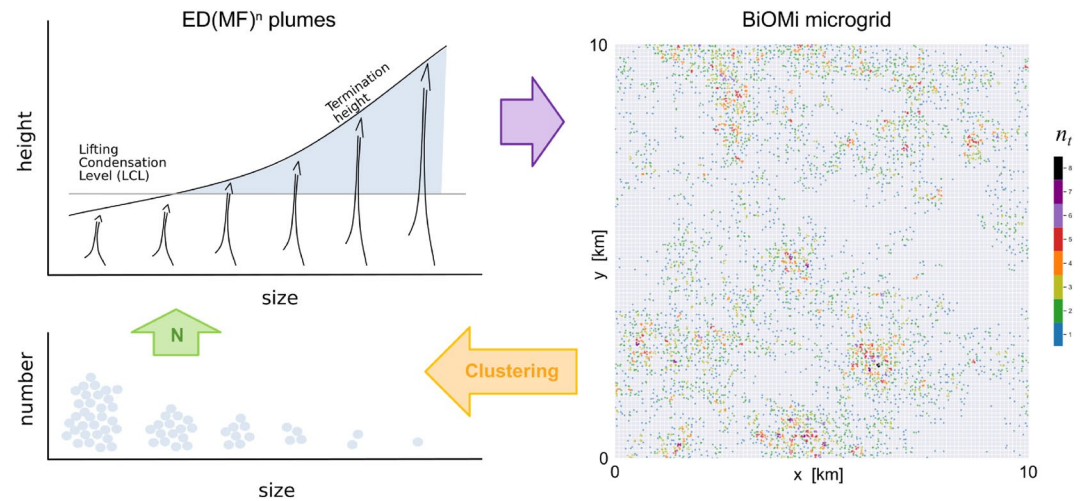
Figure 2. Schematic illustration of the coupling of Binomials On Microgrids (BiOMi) (right) and ED(MF)^n (top left) through an online clustering algorithm (bottom left). The colored arrows indicate the information flow between components, as explained in the text. n_t represents the total number of thermals in a BiOMi microgrid cell (colored).

its lifting condensation level and becomes a cumulus cloud. The two rules above are designed to capture this kind of clustering behavior and its effect on the environment.

Because only elemental processes such as object births, movement, and rules of interaction are parameterized, the framework allows an organic, bottom-up development of larger-scale clusters on the grid. The emergence and time development of these long-lived clusters is a form of memory that is carried by the grid. In this application this can be interpreted as convective memory, while the spatial distribution of clusters represents organization. An example of thermal clustering in BiOMi under these rules is shown in Figure 2. It is interesting to interpret this behavior in the context of self-organizing criticality (Bak et al., 1987). In principle, BiOMi includes the key ingredients to produce this behavior, such as a slow external driver (thermal birth), threshold-based activity and avalanches (through the rules of interaction between thermals), and a slow loss mechanism (the limited thermal life time). Indeed, NG21 showed that BiOMi exhibits scale-invariant behavior in its cluster size distribution, expressed as powerlaw scaling. More insight will be provided by the evaluation of BiOMi against LES results in Section 5.

In this study, two simple models for the reference thermal birth rate $\dot{B}$ are explored. The simplest possible model used in the control experiment is to assume it constant with time. While probably not being very realistic, the model is both sufficient and practical for testing the feasibility of the new framework. Sufficient, because it already allows spatial clustering on the microgrid to impact transport. Practical, because it keeps complexity to a minimum, thus making the behavior of the whole system easier to understand. A sensitivity experiment with a more realistic thermal birth model is also conducted that includes a diurnal cycle (as described in Section 5.5).

2.2. ED(MF)^n

The Eddy-Diffusivity multiple Mass Flux scheme or ED(MF)^n is a discretized spectral plume model formulated in size-space. As described in detail by Neggers (2015), hereafter referred to as N15, at its foundation is the size distribution of coherent convective structures in the boundary layer that are driven by the surface buoyancy flux (Brient et al., 2019; Griewank et al., 2021). These size distributions are discretized, and the vertical profiles associated with each size-bin are estimated independently by means of a rising plume model. A schematic illustration of this concept is shown in Figure 2. Individual plumes can condense and form convective clouds, and produce precipitation through simplified microphysics.

An important consequence of adopting this discretized spectral approach is that bulk (mass) flux closures are avoided. Bulk transport, meaning all transport in the gridbox, can now simply be diagnosed from the reconstructed PDF of independent plume properties. This amounts to a *decentralized* closure approach, with the individual size-bins acting as independent nodes, instead of reliance on a single, central top-down bulk closure
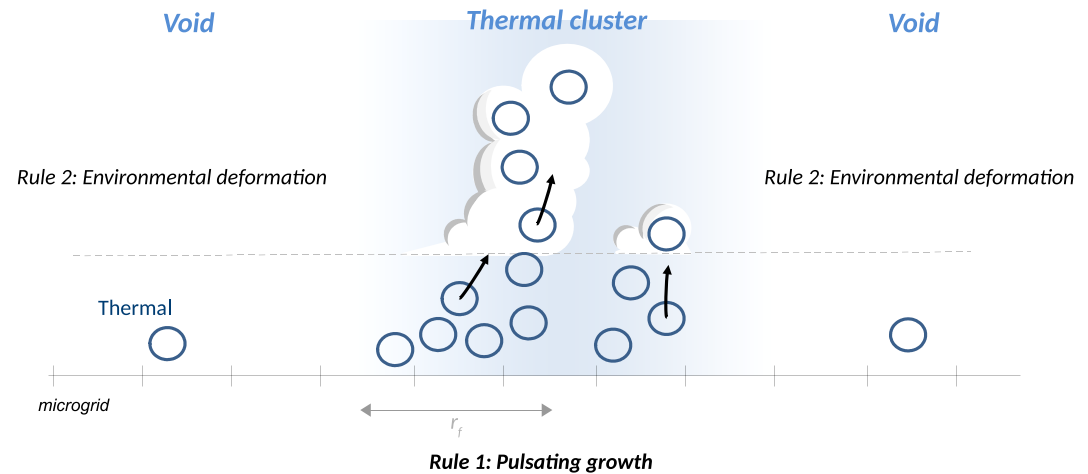
Figure 3. Schematic illustration of the role of Binomials On Microgrids (BiOMi) Rules 1 and 2 in creating long-lived thermal clusters on the microgrid. The impact radius r_f of Rule 1 is indicated for the central microgrid cell, with the associated magnitude f_p indicated by the blue background shading.

relation (Tiedtke, 1989). As explored by N15, this already introduces internal feedback mechanisms between plumes of different sizes that play a key role in equilibrating a moist convective layer, and in establishing its typical vertical thermodynamic and cloudy structure.

While a decentralized approach avoids bulk formulations, the closure problem moves to a different variable, the size distribution of plume number. N15 used a prescribed powerlaw distribution, for simplicity. In this study, we take the next step, by diagnosing the EDMF plume number distribution from the thermal distribution on the BiOMi microgrid. This concept is illustrated as the orange arrow in Figure 2. The thermal clusters are here assumed to represent coherent convective plumes. In this coupled setup, BiOMi thus functions as a "plume generator" for EDMF transport. Their coupling also makes the MF transport directly dependent on the spatial organization and memory carried by the clusters that live on the microgrid.

Another consequence is that the total area covered by MF plumes is no longer necessarily constant, a key assumption in the classic EDMF approach (Siebesma et al., 2007). With this step, we follow various recent EDMF (Cohen et al., 2020; Lopez-Gomez et al., 2020) and two-fluid modeling studies (Shipley et al., 2022; Thuburn et al., 2018; Weller & McIntyre, 2019). Note that both one-way and two-way coupling modes are possible in this framework, in principle allowing EDMF to in turn impact the microgrid (purple arrow). In this proof-of-concept study, only the one-way configuration will be explored.

2.3. Coupling

Coupling $ED(MF)^n$ to BiOMi necessitates two additional steps. The first is to adopt an online clustering algorithm, to calculate the size distribution of coherent thermal clusters on the microgrid at each EDMF time step. First, a mask I is calculated at each microgrid location, defined as

$$I = \begin{cases} 1 & \text{for } n_t \geq n_c \\ 0 & \text{otherwise,} \end{cases} \tag{5}$$

with n_t the number of thermals present in each cell and n_c a threshold value (to be calibrated next). Then, clusters are defined as areas of adjacent cells with $I = 1$, with sideway contacts included and diagonal contacts excluded. The resulting clusters are then sorted on size into a histogram, its discretization exactly matching the one adopted in $ED(MF)^n$ for consistency. Determining threshold n_c is part of the framework calibration, described in detail in Section 3.

The second step is to refine the plume vertical structure adopted in $ED(MF)^n$. N15 formulated the fractional area covered by all plumes in size-bin i as

$$a_i \;=\; \frac{N_i \; \Lambda_i \; l_i^2}{A} \qquad (6)$$

where l_i is the size of plume i, A is the horizontal area covered by the grid cell, N_i is the number of plumes in the bin, and Λ_i is a vertical structure function. For simplicity, N15 adopted cylindrical plume shapes, implying a constant Λ_i, with the horizontal area of each plume being l_i^2 at all heights. We here refine the vertical structure within the turbulent mixed layer as follows,

$$\Lambda_i(z) = 1 + C_i \; \min\left(1, \frac{z}{h}\right), \qquad (7)$$

where h is mixed-layer depth. Factor C_i expresses the relative change of plume area fraction across the mixed layer, and can be size dependent. Note that above h the plume area fraction a_i is still constant. However, with individual plumes stopping at different heights above cloud base, the total plume area will still decrease with height (as described by N15).

Relation Equation 7 reflects findings of various classic and recent studies. Lenschow and Stephens (1980) reported increasing plume diameters with height based on aircraft measurements in convective mixed layers. Using LASSO LES results, Griewank et al. (2021) found that the area decreases with height for smaller plumes but increases for larger ones, in particular plumes that rise out of the mixed layer as saturated cumulus updrafts. This behavior is also known from deep convection (Mulholland et al., 2021). The increase in plume area represents *deep rooting* and is a form of dynamic entrainment (de Rooy et al., 2013; Houghton & Cramer, 1951). One of the main outcomes of this study is that deep subcloud rooting for large plumes is essential for making spectral transport schemes work when coupled to realistic plume number densities. This is further described in results Section 5. The calibration of C_i against LES data is described in Section 3.

3. Calibration

The framework is calibrated at two points. The first concerns the two parameters $\left\{\dot{B}, n_c\right\}$ representing the BiOMi thermal birth rate and the clustering threshold used in the coupling to $ED(MF)^n$, respectively. To this purpose, the total area fraction covered by thermals is used as a constraint, as illustrated in Figure 4. For a given combination of $\left\{\dot{B}, n_c\right\}$, the total cluster area fraction A_c quickly equilibrates. This expresses a stable balance between the slow driver and loss processes. The phase space diagram shown in Figure 4b indicates that a well-defined 1-to-1 relation exists between a set of values for these parameters and A_c. This implies that we can calibrate the coupling in such a way that a specific, low area fraction is obtained that is similar to previous EDMF studies. In practice, we choose $A_c = 15\%$ and $n_c = 2$, which corresponds to a birth rate $\dot{B} = 2e^{-7}$ m^{-2} s^{-1}. Note that this fraction covers all clusters, including both saturated and unsaturated ones.

The second point of calibration concerns the plume vertical structure Λ_i. The vertical structure of the $ED(MF)^n$ plumes are calibrated to match the structure of the convective objects Griewank et al. (2021) detected within LES simulations. Calibration is done with data from 11 June 2016 at the ARM SGP site, the characteristics of which are described in more detail in Section 4.

Griewank et al. (2021) detect convective objects in 3D snapshots as volumes of spatially connected gridboxes with the aid of a surface-emitted scalar that decays over time (Couvreux et al., 2009). They found that objects that have a base below 100 m height and a vertical extent exceeding 100 m contribute a majority of the vertical transport. These objects are conceptually consistent with the surface-rooted convective plumes as defined in $ED(MF)^n$. The example plume shown in Figure 1 is one of the objects detected by Griewank et al. (2021), with the object outline indicated.

Figure 5 shows the change in a_i across the subcloud mixed layer as a function of object size, as sampled from the LES of 11 June 2016 at a 30-min frequency resulting in a total of thirty thousand objects. A robust and well-defined dependence on object size is apparent, with the area of large objects significantly increasing toward mixed layer top. In contrast, small objects actually lose mass, pointing at significant detrainment within the

a)

b)
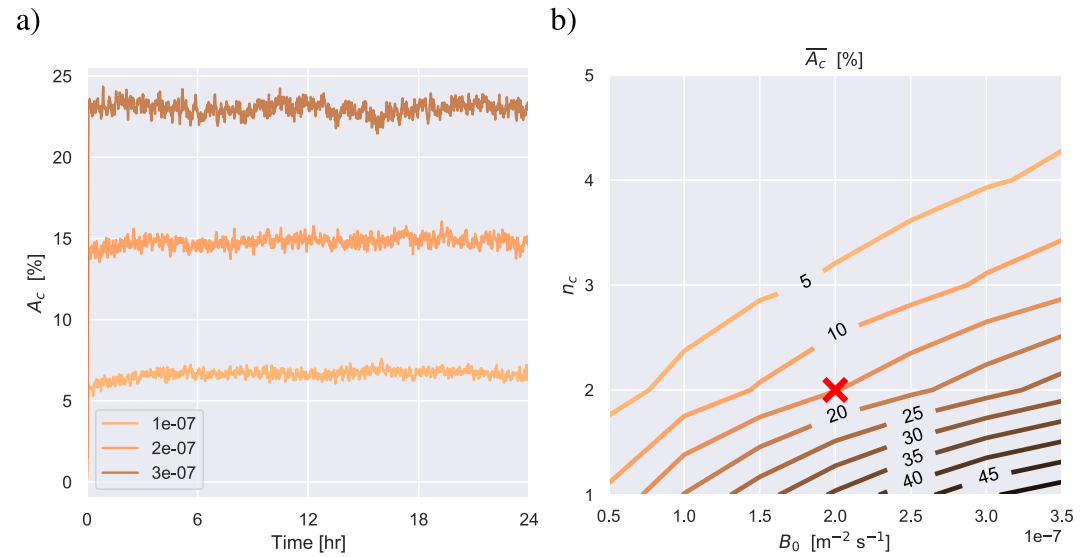
Figure 4. Results from offline experiments with Binomials On Microgrids (BiOMi) on a 100×100 grid. (a) Time series of total cluster area fraction A_c for $n_c = 2$ and for three experiments with a different $\dot{B}$ value. (b) Phase-space diagram of time averaged $\overline{A_c}$ (contoured) as a function of thermal birth rate $\dot{B}$ and clustering threshold n_c. The thermal life time τ is always 300 s. The red marker in (b) indicates the values selected in this study.

mixed layer. The Pearson correlation coefficient associated with this data is 0.86. Applying a linear fit yields the following calibration for C_i,

$$C_i = -1 + 0.00142 \ l \tag{8}$$

we find that adopting a mixed-layer-deep rooting structure for large plumes proves necessary to make EDMF work when coupled to an evolving, more realistic cluster population as sampled from the BiOMi microgrid. This insight will be discussed in detail in Sections 5 and 6.
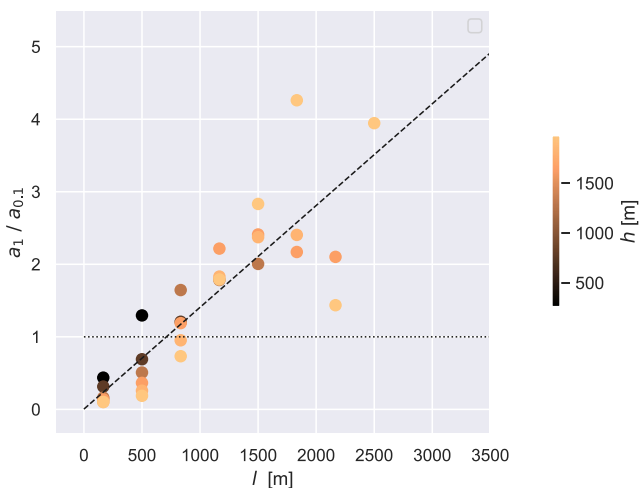
Figure 5. Ratio of cluster area at mixed layer top versus that at surface layer top, as a function of cluster size l, as sampled in a LASSO LES of shallow cumulus observed on 11 June 2016 at the Atmospheric Radiation Measurement Southern Great Plains site. The data points represent averages over 2 hours at a bin-width of 333 m, with the color indicating mixed layer depth h. The Pearson correlation coefficient is 0.86. The black dashed line indicates the least squares linear fit.

4. Experimental Design

4.1. Implementation

To perform SCM experiments with the coupled BiOMi-ED(MF)^n system, it is implemented as a subgrid scheme into the Dutch Atmospheric Large-Eddy Simulation code (DALES, Heus et al., 2010). The long-term goal of this effort is to be able to use the LES code also as a simple larger-scale circulation model, so beyond its common high-resolution range. This study is only the first step in this process, using the DALES code in a limited 1×1 grid setting. The LES grid is hereafter referred to as the *macrogrid*, to clearly distinguish it from the BiOMi microgrid. In practice, the buoyancy, pressure gradient, horizontal advection, and horizontal diffusion terms are all switched off in the corresponding prognostic governing equations as resolved and time integrated in the LES code.

To implement the coupled BiOMi-ED(MF)^n scheme, the method described by Brast et al. (2018) is adopted. Within the convective layer, the ED component replaces the vertical diffusion of the LES subgrid scheme, maintaining the LES diffusion model above. All EDMF variables are calculated based on the mean state vertical profiles of the macrogrid and the surface (flux) boundary condition, provided as input. EDMF has its own solver, providing tendencies of prognostic variables (θ_l, q_t, u, v) back to the macrogrid. The BiOMi scheme is time integrated independently at its own constant time step,

a)   b)
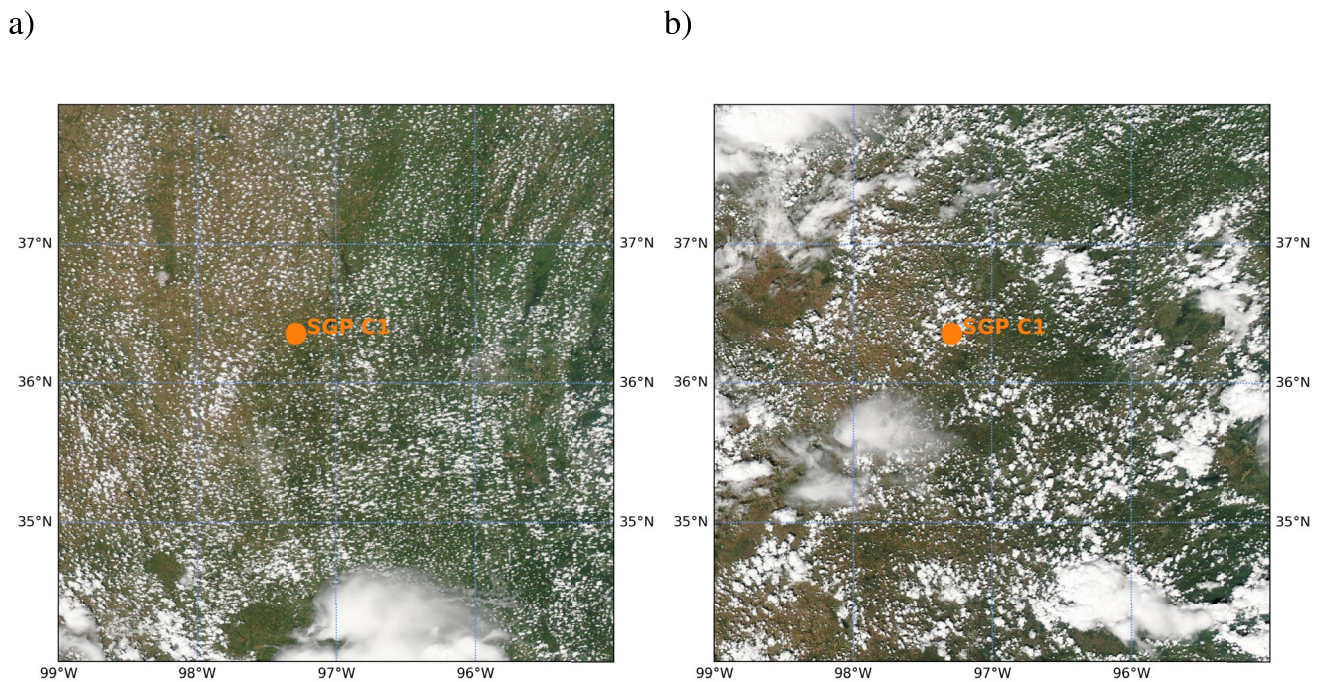
Figure 6. MODIS Aqua corrected reflectance (true color) images of shallow cumulus cloud populations in the Atmospheric Radiation Measurement Southern Great Plains area on (a) 11 June 2016 and (b) 30 August 2016. NASA EarthData obtained through the Global Imagery Browse Services.

while the EDMF module follows the Runge-Kutta time stepping routine as applied by default in the LES code. The latter is modified to allow GCM-like time increments; more precisely, the Peclet time step limiter no longer sees the vertical diffusion, as this process is now carried out by the EDMF subgrid scheme.

4.2. LASSO Cases

Two shallow convective days at the ARM SGP site (Mather & Voyles, 2013; Stokes & Schwartz, 1994) are selected for the SCM experiments. Figure 6 shows MODIS Aqua true color satellite images of the clouds on 11 June and 30 August 2016. On both days, the shallow cloud population shows simple forms of spatial organization, which can be considered typical for this continental low cloud regime (Neggers et al., 2019). On 11 June the field is relatively homogeneous, with a hint of street formation, while on 30 August a distinct mesoscale pattern is visible, with some arc-like structures hinting at cold pool presence. The latter case was recently investigated in more detail by Chen et al. (2020). Both days are part of the library of cases as simulated at cloud-resolving resolution within the ongoing LASSO project (Gustafson et al., 2020). The 30 August case was also part of the Hi-SCALE field campaign (Fast et al., 2019). These days are selected because of their similarities but also their differences. Both days share a well-defined diurnal cycle in boundary-layer structure, featuring a gradually rising cloud base height and a distinct second phase in the cloud layer deepening in the later afternoon. On 30 August the cloud layer was deeper throughout the day, and featured more precipitation. We selected these days to find out if BiOMi-ED(MF)^n can reproduce both the shared basic diurnal cycle as well as the observed differences.

To perform the SCM simulations for these 2 days, the large-scale forcings and boundary conditions at the C1 observatory as part of the LASSO V2 Alpha Release are used (Gustafson et al., 2017b). This data bundle is described in detail by Gustafson et al. (2017a). The simulations are initialized at 06:00 local time (LT) and cover the full daytime convective period. Time-dependent large-scale forcings and boundary conditions are applied. The forcings are horizontally homogeneous, consisting of (a) prescribed tendencies due to horizontal advection and (b) vertical advection consisting of the product of a prescribed profile of large-scale subsidence and the vertical gradients of the horizontally averaged simulated state variables. Geostrophic wind forcing is also applied. The surface sensible and latent heat fluxes are prescribed and time dependent. While this excludes land-atmosphere feedbacks, the time-dependent solar forcing of the boundary layer is captured this way. This configuration has

Table 1
Overview of the Model and Grid Configuration as Applied in the ED(MF)^n Experiments Conducted in This Study, as Described in Section 4.4

BiOMi		
l_t	Thermal size	100 m
τ	Thermal life time	300 s
$\dot{B}$	Thermal birth rate	$2e^{-7}$ m^{-2} s^{-1}
C_f	Impact factor in Rule 1	2,000
r_f	Impact radius of Rule 1	300 m
$k_x \times k_y$	Microgrid size	$1,000 \times 1,000$
$\Delta x \times \Delta y$	Microgrid cell size	100×100 m^2
Δt	Integration time step	60 s
ED(MF)^n		
$\{a, b, \mu\}$	Constants in plume kinetic energy budget	$\{0.75, 1, 0\}$
ϵ	Plume lateral entrainment rate	$1/l_p$
Coupling		
n_c	Clustering threshold (thermal number)	2
DALES		
$K_x \times K_y \times K_z$	Macrogrid size	$1 \times 1 \times 256$
$L_x \times L_y$	Macrogrid cell size	100×100 km^2
L_z	Macrogrid cell depth	25 m
Δt	Integration time step	300 s

successfully been applied in the past to simulate diurnal cycles of shallow cumulus over land (Brown et al., 2002).

4.3. Evaluation Data Sets

The main goal of the evaluation is to provide proof of concept of the newly proposed coupled microgrid-transport framework. We will judge the proposed framework on its ability to reproduce the mean structure of the evolving shallow cumulus topped boundary layer, with a basic agreement being sufficient to pass the test. For evaluation, we rely on routine ARM observational data sets combined with selected output from LASSO LES experiments.

The ARM-interpolated sonde data set provides information about the vertical thermodynamic structure at the C1 observatory of the SGP site (Jensen et al., n.d). This data set is routinely generated and represents a combination of multiple sounding instruments, provided at a time resolution of 1 min. Of this data set, the profiles of potential temperature and water vapor-specific humidity are used. The second ARM data set is the time-gridded convective cloud base height product as part of the LASSO Alpha 2 Data Bundles (Gustafson et al., 2017a, 2017b). The time discretization of this data set is 1 hour, which is fine enough to sample the diurnal evolution of the lower boundary of the cumulus cloud layer.

Output from LES experiments supplements the observational data sets for the two selected days, consisting of reruns with the MicroHH code (van Heerwaarden et al., 2017) as recently described by Neggers et al. (2019) and Griewank et al. (2021). The reference LASSO V2 setup is adopted, which has been thoroughly evaluated against observations (Gustafson et al., 2020). The horizontal domain size is 25.6×25.6 km^2, spatially discretized at 25×25 m^2. Apart from mean state variables, results from the clustering analysis performed by Griewank et al. (2021) are used to calibrate the scheme (as described earlier in Section 3) but also to evaluate the convective population statistics of BiOMi-ED(MF)^n.

4.4. Model Setup

The control settings of the BiOMi-ED(MF)^n framework as implemented in DALES are summarized in Table 1.

The DALES macrogrid has a size of $1 \times 1 \times 256$ with cell dimensions of 100 km $\times$ 100 km $\times$ 25 m. This cell size is here assumed large enough to exclude boundary-layer gray zone effects, with the shallow convective cloud population more or less fully sampled (Neggers et al., 2019). This domain size also matches the scale at which the LASSO large-scale forcings are estimated. Following this setup, the diurnal cycle of solar forcing is imposed through a prescribed surface sensible and latent heat flux. Interactive radiation is used, which only sees the evolving macrogrid state. This means that any EDMF subgrid cloudiness does not yet affect radiative transfer. For the highly transient continental diurnal cycles of shallow convection considered here, the tendencies associated with convective transport are typically much larger than any radiative tendencies. This motivated early LES studies to operate without interactive radiation (Brown et al., 2002). In these experiments, the mean state always stays subsaturated, and "resolved" clouds do not form on the macrogrid.

BiOMi thermals have a size $l_t = 100$ m and a lifetime of $\tau_t = 300$ s. The microgrid size is $1,000 \times 1,000$ with a cell size of 100×100 m^2. The integration time step is constant at 60 s, yielding $\tau_t/\Delta t = 5$ discrete age strata in the thermal demographics. Constants $\{B, n_c\}$ result from the scheme calibration as described in Section 3. For ED(MF)^n the N15 setup is in principle adopted, with a few exceptions. For the plume kinematic energy budget, the settings as recommended by de Roode et al. (2012) are used, with constants $a = 1$, $b = 1.5$, and $\mu = 0$. Plumes of all sizes are initialized identically via coupling to the surface heat fluxes through surface similarity. The lateral mixing or dilution rate ϵ is assumed to be inversely proportional to plume size l_p, as reported by N15 and a range of other studies (Mulholland et al., 2021; Peters et al., 2020; Simpson & Wiggert, 1969; Turner, 1962).

Table 2
Overview of the Conducted ED(MF)^n Experiments

Label	Number density model	Plume vertical structure
PP_a	Prescribed Powerlaw with $k = -2.74$	Constant: $\Lambda = 1$
B_a	BiOMi with $\dot{B} = 2e^{-7}\,\mathrm{m}^{-2}\,\mathrm{s}^{-1}$	Constant: $\Lambda = 1$
B (control)	BiOMi with $\dot{B} = 2e^{-7}\,\mathrm{m}^{-2}\,\mathrm{s}^{-1}$	Dependent on (z, l) following Equations 7–8
B_m	BiOMi as **B**, thermal redistribution at $t = 12$ LT	"
B_θ_v	BiOMi with $\dot{B} \sim F_b^s$	"

Note that other proposed mixing models could easily be tested in this framework, for example, dependencies on vertical velocity (Drueke et al., 2021; Neggers et al., 2002). The ED(MF)^n trigger condition of a positive surface buoyancy flux is maintained, which for these continental cases means that between sunset and sunrise the EDMF transport shuts down.

4.5. Conducted Experiments

Table 2 contains an overview of the SCM experiments with ED(MF)^n conducted in this study. The **PP_a** experiment represents the default N15 configuration of ED(MF)^n, and is included for reference. **PP_a** uses a prescribed and time-constant single-powerlaw distribution is adopted for the plume number density $N_i(l)$, without a scale break and having exponent $k = -2.74$, and covering a size range up to 2 km. The plume area $a_i(z)$ is constant with height in the mixed layer, as indicated by subscript a.

Experiment **B_a** applies the same setup, with the exception that $N_i(l)$ is diagnosed from the BiOMi microgrid, using a prescribed thermal birth rate $\dot{B}$. The third experiment **B** acts as the control experiment, representing the "best setting" for coupling transport to the thermal population on the microgrid. It only differs from B_a in that a_i can vary with height across the mixed layer (Relation 8). Together, these experiments provide insight into the impact of coupling convective transport to a realistic and evolving thermal population, and into the changes required in the plume vertical structure to make this work. No extra calibration was undertaken for experiments **B_a** and **B**; apart from the stated changes, all model settings are identical to those of **PP_a**.

The final two experiments **B_m** and **B_θ_v** are sensitivity tests based on control experiment **B** that are designed to investigate key aspects of the model behavior. These will be discussed in detail in Section 5.5.

5. Results

5.1. Mean State

Figure 7 shows the vertical structure of the boundary-layer clouds and its time development on both days in the control experiment B with BiOMi-ED(MF)^n. On both days, the general structure and evolution of the convective cloud layer as visible in the LES are reproduced to a reasonable degree. This includes the gradually rising cloud base, as well as the double deepening phase as expressed in the cloud top height. The defining differences between the two cases are also captured to a satisfactory degree, such as the lower cloud base and higher cloud top on 30 August. However, some small deviations also exist, such as a slightly too early cloud onset.

A more detailed evaluation of the EDMF cloud boundaries is conducted in Figure 8, and also includes observed cloud base heights. These time series highlight that on both days cloud base rises quickly after cloud onset, and levels off after about 14:00 LT. This behavior is well captured by the LES. Cloud top height also rises quickly after cloud onset, but experiences a well-defined second deepening phase, also after 14:00 LT. BiOMi-ED(MF)^n satisfactorily reproduces both these characteristic features, including differences in cloud layer onset, height, and depth between the 2 days. For 30 August, the cloud layer depth is briefly overestimated immediately after cloud onset.

In general, both the contour plots and time series display smooth time evolution of the coupled BiOMi-EDMF system. There is no sign of artificial intermittency, instabilities, or discrete behavior. This indicates good quasi-equilibration at small time scales. N15 showed that this is partially due to the cumulus valve and
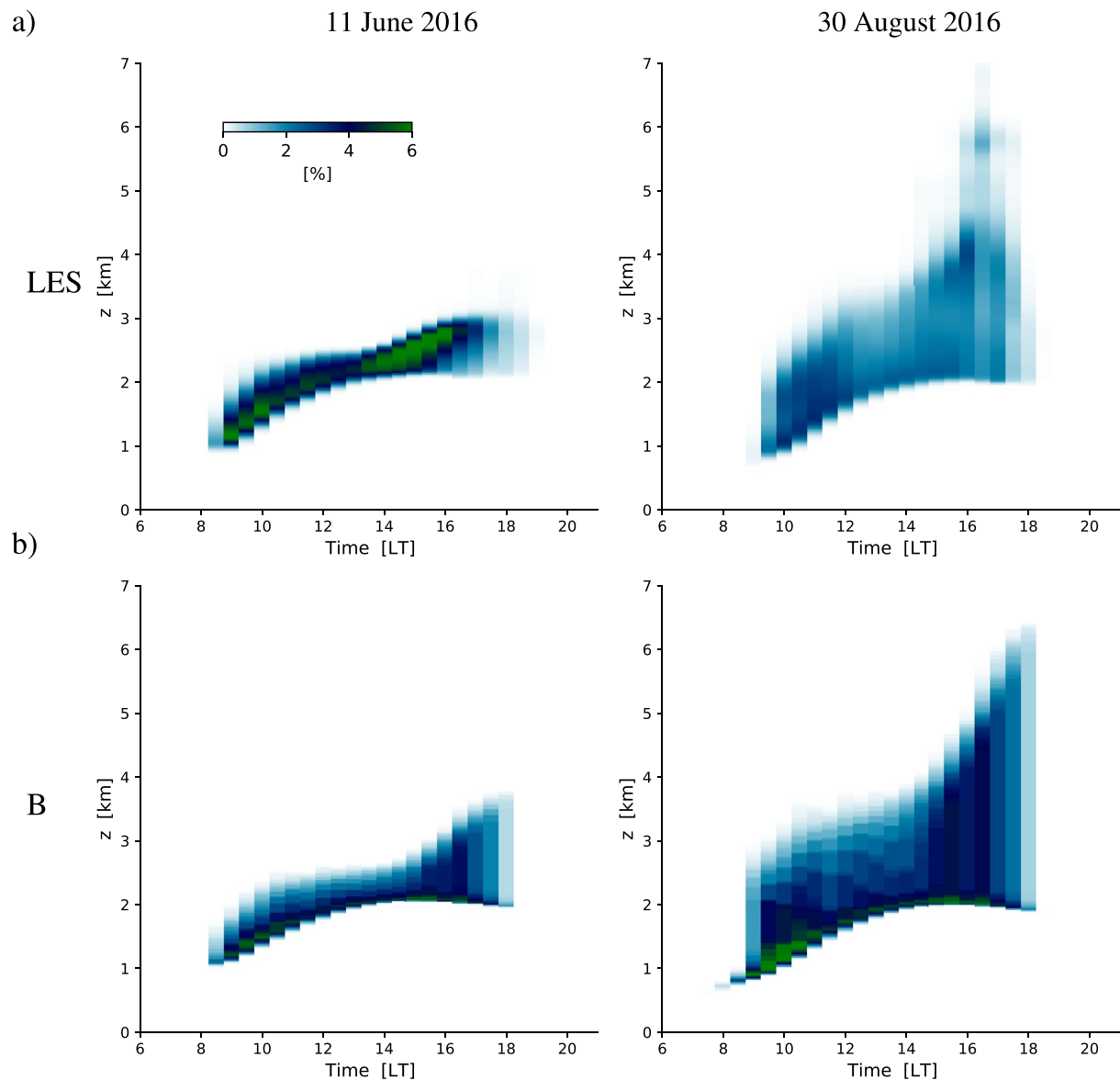
Figure 7. Time-height raster plots of cloudy area fraction in (a) LES and (b) BiOMi-ED(MF)^n control experiment B. The left column shows results for 11 June 2016, the right column for 30 August 2016. For LES, the cloud core fraction is shown (defined as all cloudy point that are rising and have positive buoyancy), for EDMF, the condensed plume fraction. The data gridding represents 30 min averages.

acceleration-detrainment mechanisms that are captured by ED(MF)^n through system-internal feedbacks. Apparently, the coupling of ED(MF)^n to the evolving cluster population on the microgrid does not introduce instability, which is worth noting. The smooth behavior also reflects that the microgrid covers a large domain (100×100 km^2). This avoids any intermittency due to subsampling of the plume population, a gray zone effect i.e., by design not considered in these experiments.

More insight into the boundary-layer vertical structure is provided by Figure 9, showing vertical profiles of the mean thermodynamic state and cloud core fraction at 12:00 LT. There are some small differences between LES and the ARM radiosonde profiles, here shown for reference. However, in general, the vertical structure of the cumulus-capped boundary layer is satisfactorily reproduced in these simulations. Note that the B experiment is forced in exactly the same way as the LES, so its comparison to the LES profiles is most meaningful. The amplitude and structure of both the thermodynamic state and the convective area fraction are well reproduced by BiOMi-ED(MF)^n. In the cloud core profile, the artifact of the discretization of the plume size density is visible, in
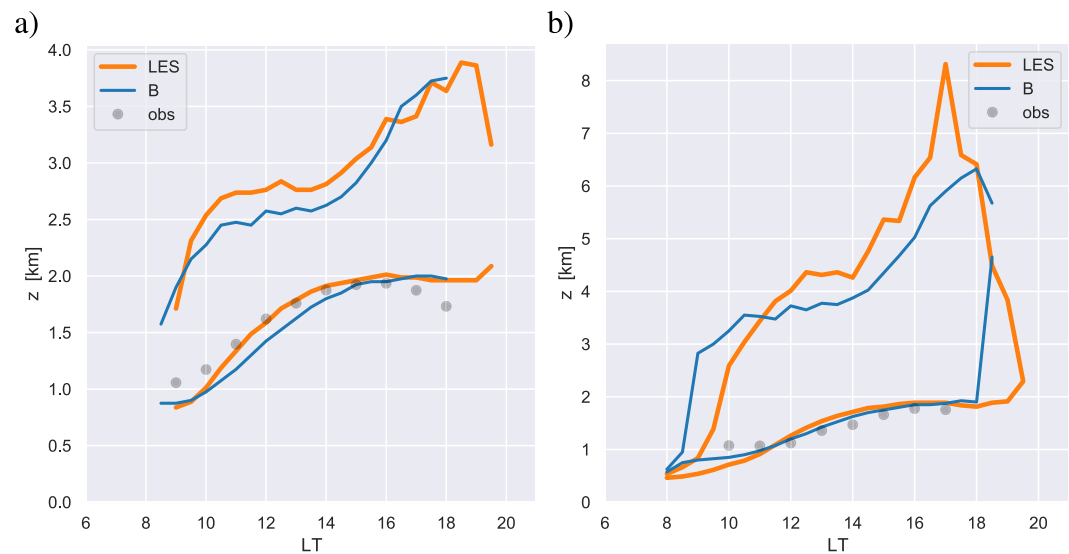
Figure 8. Time series of cloud base and top height (a) 11 June 2016 and (b) 30 August 2016. The control experiment B is shown in blue, the LES results in orange, and the gridded observations as part of the LASSO Data Bundle (v2) as gray dots.

the shape of the stepwise decrease with height reflecting the variation in termination height among the saturated plumes in ED(MF)^n. The biggest differences with LES exist on 30 August, with a slight dry bias in the cloud layer and a weak moist bias above the inversion.

5.2. Cluster Population Statistics

The properties of the cluster population on the BiOMi microgrid are considered next. To simplify the analysis, we only focus on 11 June 2016, because this day had no surface rain to speak of. The convection on 30 August was much deeper and featured significant precipitation, which likely affected the mesoscale organization. Such impacts of rain on the spatial organization are not present yet in BiOMi's rules of thermal interaction, making its clustering most comparable to no-precipitation conditions.

The development of spatial clustering on the BiOMi microgrid is illustrated in Figure 10, showing snapshots of the microgrid at three time points during the day. The masking as part of the online cluster algorithm as described in Section 2.2 is also shown, as expressed by the coloring of the clusters. Cluster size and spacing start out small, but gradually increase, with the clusters becoming surrounded by areas that are increasingly void of thermals. The first snapshot can be loosely compared to the satellite image for this day, as shown in Figure 6a. While the observed spatial distribution of many small and few larger cumulus clouds seems well captured, the weak organization into cloud streets is absent. The likely reason for this is that the rules of interaction in BiOMi are not yet aware of wind shear, which is known to create such streets.

A more detailed evaluation of population statistics is performed by considering size distributions of cluster number as produced by BiOMi. These are shown in Figure 11, at various points during the B_1 experiment of 11 June 2016. The well-defined scaling range in the number size distribution as diagnosed in the LES is satisfactorily reproduced. The associated power law exponent in BiOMi is −2.74, which is very close to the exponent diagnosed in LES (−2.77). The presence of a cut-off or scale break above which the cluster number sharply decreases with size is also captured. The scaling range becomes wider with time, with the cut-off point gradually moving toward larger sizes.

Both the presence of a scaling range and a cut-off or scale break are well-known expressions of self-organizing criticality (Bak et al., 1987), and have been reported in previous studies of shallow cumulus populations (Neggers et al., 2003; van Laar et al., 2019) and deep precipitating convection (Quinn & Neelin, 2017). The emergence of these features on the BiOMi microgrid suggests that the two simple rules of interaction, combined with a prescribed thermal birth rate and life time, are already sufficient to reproduce this behavior. We speculate that under these two rules, thermal clusters first need to reach a certain critical size or mass before being able to
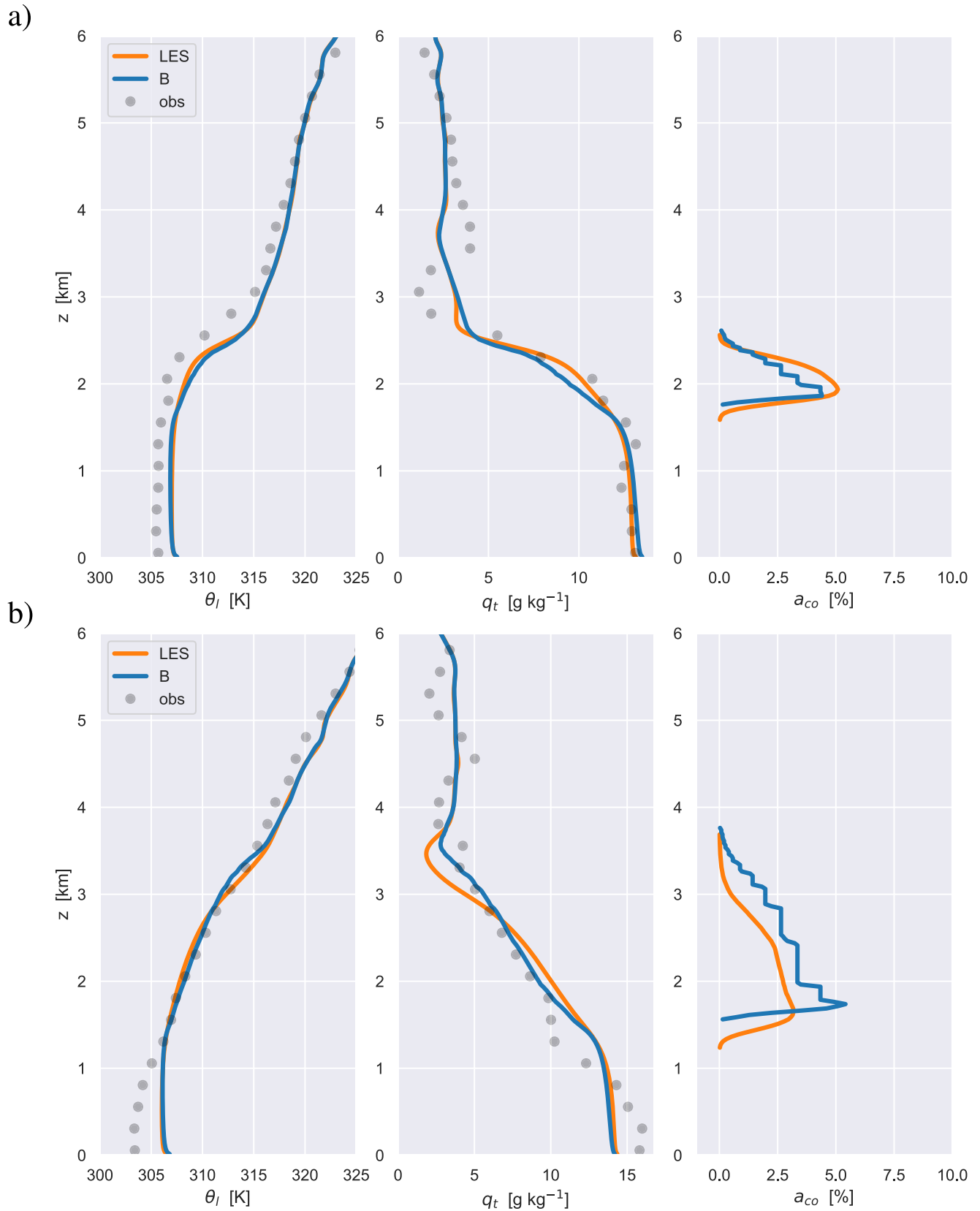
Figure 9.

sufficiently sustain themselves with new thermals (rule 1) as well as effectively suppress thermal births around them (rule 2). Only then can these clusters survive, live longer, and grow further. This apparent size threshold is thus responsible for causing the phase transition and the scale break. The threshold is likely dependent on the presence of other large clusters in the domain, which similarly perturb the p field. Because these clusters need time to develop, this threshold is time dependent.

5.3. Spatial Organization and Convective Memory

The time evolution of two spatial characteristics of the BiOMi cluster population is assessed in Figure 12. These properties reflect spatial organization, and their time development can be interpreted as expressing convective memory on the microgrid. The size of the largest cluster in the domain is shown in Figure 12a. In the LES, it gradually increases during the day, from about 500 m after sunrise to about 2,000 m at sunset. This behavior is consistent with previous LES studies (van Laar et al., 2019). BiOMi reproduces this trend to the first order; only during the first 4 hr it seems to slightly overestimate the scale growth as it happens in the LES.

Closely related to the maximum cluster size is the spatial organization on the microgrid. This can be expressed by means of the I_{org} metric (Tompkins & Semie, 2017), which differentiates between regular ($I_{org} < 0.5$), random ($I_{org} = 0.5$) and clustered ($I_{org} > 0.5$) distributions of objects on a two-dimensional plane. Once the initial spinup has occurred, the LES results shown in Figure 12b indicate a gradual shift from randomly distributed clusters early on toward spatially organized clusters in the late afternoon (Neggers et al., 2019). Despite a weak overall overestimation of the degree of clustering, BiOMi captures this gradual trend. This suggests that the BiOMi control experiment already captures the basic process of spatial organization in diurnal cycles of continental shallow convection, despite using a simple constant thermal birth rate. In this setting, the increase in largest cluster size can only happen through population-internal processes introduced by the two rules of thermal interaction. As discussed by NG21, this process takes time, and is an expression of convective memory i.e., stored on the grid. In Section 5.5, a sensitivity test is discussed that shows that the gradual cluster growth is indeed a memory effect.

5.4. Impacts of the Scale Break

A key novelty introduced by coupling EDMF to BiOMi is that the spatial organization on the microgrid as described in the previous section can now impact convective transport, through the number density of MF plumes. As a consequence, this size distribution now no longer follows a prescribed single powerlaw. Instead, it now features a distinct and well-defined scale break, which progresses toward larger sizes during the diurnal cycle (see Figure 11). The comparison to LES also confirms that the scale breaks produced by BiOMI are realistic for these cases. What the scale break expresses is that the plumes above the scale break occur much less frequently compared to a single powerlaw setup. This is expressed nicely by comparing the number densities between the control experiment B and reference experiment PP_a with a prescribed powerlaw, as shown in Figure 13a. Note that the scale-break size in experiment B roughly coincides with the minimum plume size at which substantial saturation occurs (see Figure 13b).

The presence of a scale break has an important and direct impact on the associated convective transport. As described by N15, in ED(MF)^n the number of plumes N_i in size-bin i affects the kinematic plume mass flux, through the plume area fraction a_i,

$$M_i = a_i \; w_i \;\; = \;\; \left(\frac{N_i \; \Lambda_i \; l_i^2}{A} \right) \; w_i \tag{9}$$

where we substituted a_i with Relation Equation 6. The recent study of mass flux profiles in marine subtropical shallow cumulus by Klingebiel et al. (2021) has provided observational support for such proportionality of mass flux to area fraction. One understands from Equation 9 that the lower frequency of occurrence of the largest plumes in experiment B (highlighted by the orange shading in Figure 13) implies a reduced contribution to the total convective overturning. Hereafter, the size range above the scale break is referred to as the *Super-Scale-*

Figure 9. Mean state profiles at 12:00 local time of domain-averaged liquid water potential temperature $\overline{\theta}_l$ (left), total specific humidity $\overline{q}_t$ (center), and cloud core area fraction a_{co} (right) for (a) 11 June 2016 and (b) 30 August 2016. Control experiment B is shown in blue, the LES results in orange, and the vertically gridded Atmospheric Radiation Measurement interpolated sonde data as gray dots.
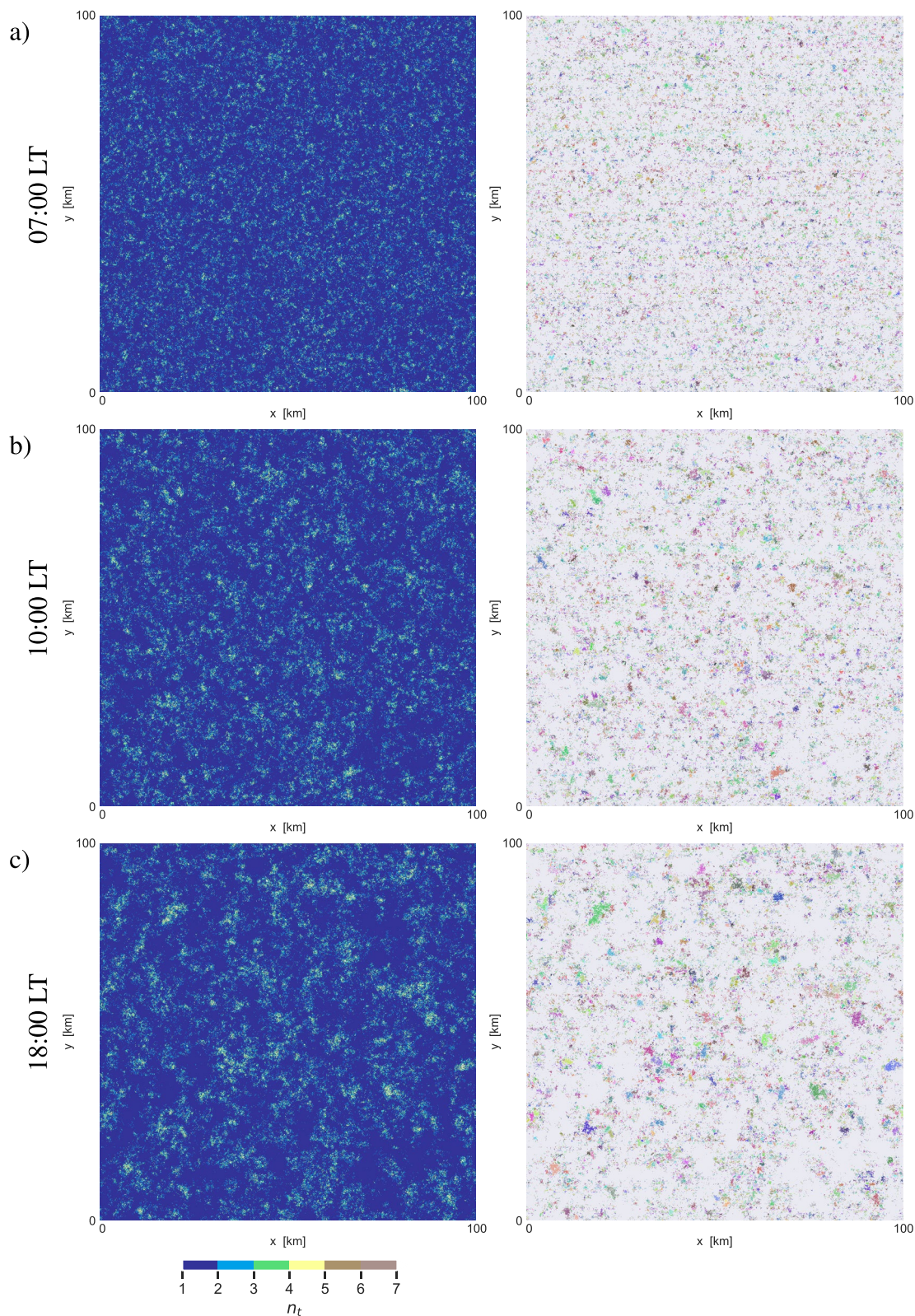
Figure 10. Snapshots of thermal clustering on the BiOMi microgrid at (a) 07:00 local time (LT), (b) 10:00 LT and 18:00 LT during the B experiment for 11 June 2016. These time points correspond to 1, 4, and 12 hr after initialization. Left column: Rasterplot of the total number of thermals per cell, n_t. Right column: The associated cluster mask, with each individual cluster given a unique color. Note that the thermal clusters represent both dry and condensed thermal plumes.
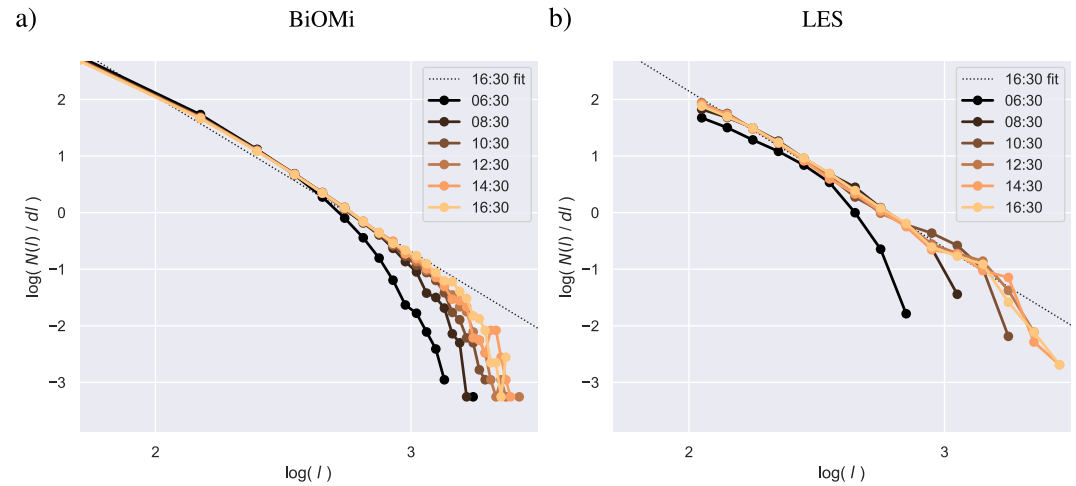
Figure 11. Log-log plot of size densities of cluster number $N(l)$ at 2-hr intervals during 11 June 2016, with size l shown in m. (a) Clusters on the Binomials On Microgrids (BiOMi) microgrid during experiment B. (b) Coherent objects in LASSO LES. Lines represent hourly means around the indicated time-point (local time) for a 100×100 km^2 domain. The dotted black line indicates the linear fit $f(l) = al + b$ in log-log space for the size densities at 16:30 local time, as applied to the scaling range $100 < l < 1,000$ m. The corresponding powerlaw exponents are $a = -2.74$ for BiOMi and $a = -2.77$ for LES.

break Size Segment (S^4 in short). Accordingly, because of the scale break we expect an internal shift in the vertical transport across the size distribution in ED(MF)^n toward smaller plumes. This is already expressed by the shift in condensation toward smaller plume sizes, as shown in Figure 13b. This internal shift likely affects the vertical structure of the boundary layer and its evolution. In particular, the coupling between the cloud layer and the subcloud layer is affected, being carried by the largest plumes in the spectrum.

Figure 14 provides more insight by comparing control experiment B to the sensitivity experiment B_a in which the plume area fraction a_i is constant with height. Note that experiments B_a and B were not individually recalibrated, and are identical to PP_a except for the modifications stated in Table 2. Both experiments B_a and B sample their plume number density from the BiOMi microgrid, and thus include a scale break. The boundary layer vertical structure in B_a shows significant biases compared to the LES. Its subcloud layer is too cold and
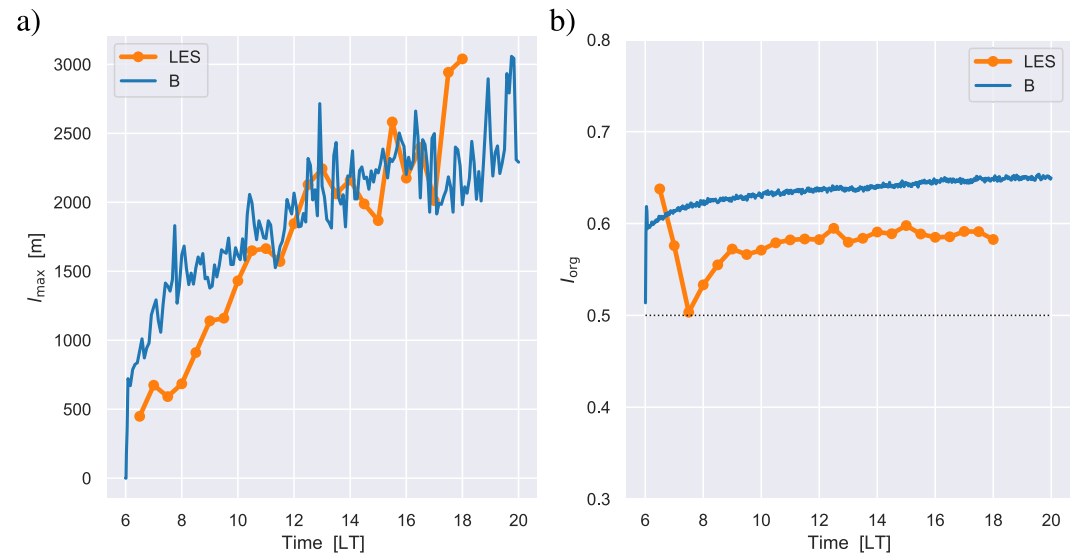
Figure 12. Time series of spatial statistics of the cluster population for 11 June 2016. (a) The largest cluster size l_{max}. (b) Organization metric I_{org}. Binomials On Microgrids (BiOMi) data for experiment B is shown in dark blue, and LES data in orange.
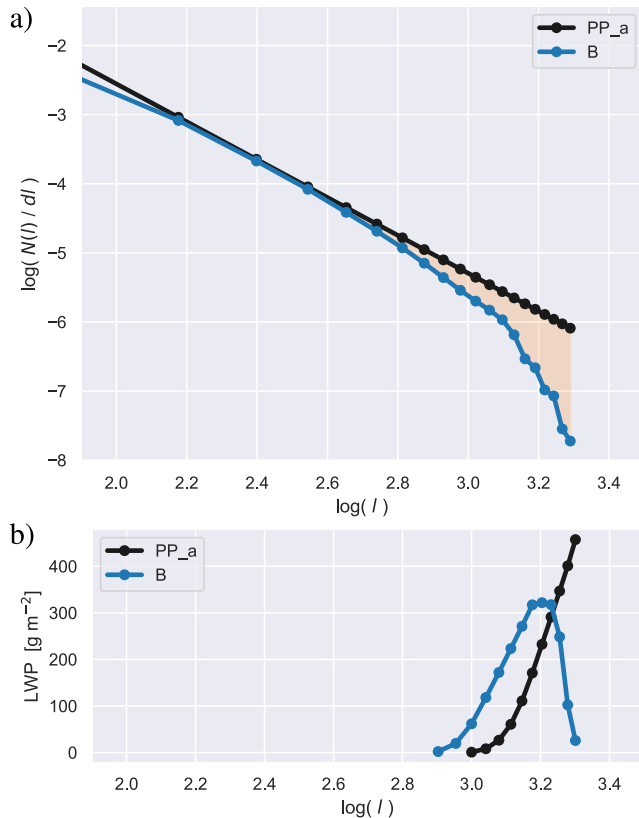
Figure 13. Size densities of (a) plume number $N(l)$ and (b) plume liquid water path for experiments B (blue) and PP_a (black) as time averaged over the period 10:00–12:00 local time on 11 June 2016. The difference in plume number at sizes above the scale break is shaded orange. This size range is referred to as the Super-Scale-break Size Segment (S^4).

moist, while the cloud layer is too warm and dry. This signal typically indicates a lack of transport or ventilation between the two layers. Because this cloud base transport is typically carried by the largest plumes, their relatively low number due to the scale break is directly responsible for this bias.

Interestingly, the reference experiment PP_a does not show these biases. As shown by N15, this default configuration of ED(MF)^n already performs satisfactorily for many other cases of moist convection. The only differences between PP_a and B are (a) the shape of the number density and (b) the plume vertical structure. This can only mean that the impact of the scale break, or the reduction in the relative number of large versus smaller plumes, must be compensated by the difference in plume vertical structure. The latter is investigated in Figure 15, showing profiles of bulk properties of the super-scale-break size segment S^4 for 11 June 2016. In LES, the area fraction a of S^4 more or less increases linearly across the subcloud layer. As discussed by Griewank et al. (2021), this structure is persistently and typically present during shallow convective conditions over land, and can be interpreted as the largest plumes "rooting" across the full subcloud layer. In other words, they drain mass not just from the surface layer ($z/h < 0.1$) but from the whole boundary layer. The constant area fractions in experiment B_a (and PP_a) are clearly not supported by these LES results. The linear increase below cloud base as adopted in experiment B is much more realistic. This shows that the calibration of C_i in Equation 8 on the same LES data was effective in correctly introducing this height dependence.

The contribution by S^4 to the total convective flux is shown in Figure 15b. The vertical flux of PP_a is much too large compared to LES throughout the mixed layer. In experiment B_a, the flux has much reduced, due to the reduction in plume number above the scale break. The increase in a with z as adopted in experiment B counters this effect, and also is in good agreement with LES. For reference, the humidity tendencies associated with the divergence of these flux profiles are shown in Figure 15c. Experiment PP_a has an erroneous peak negative tendency in the surface layer, which has much reduced in B_a and B. Adopting the linear increase in a as in experiment B

then causes the S^4 plumes to drain humidity from the whole mixed layer, not just the surface layer ($z/h < 0.1$). As a result, the humidity flux by S^4 at mixed layer top h is comparable to LES again, and the coupling between cloud- and subcloud layer has thus been restored. This is expressed by the realistic vertical thermodynamic structure of the boundary layer in experiment B (see Figure 14).

We did attempt to recalibrate configuration B_a to find out if we could remove the underestimated flux at $z = h$ this way. This mainly involved the plume lateral mixing rate, which is one of the few tuning parameters left in the ED(MF)^n transport system. However, despite our best efforts, the flux across cloud base always remained underestimated, and the associated biases in the profiles were persistent. Apparently, the reduction in the number of large plumes (as a result of the introduction of a scale break in the size distribution) has a too big, first-order impact on convective transport across cloud base. This transport can only be fully recovered when the vertical structure of the largest transporting updrafts in the mixed layer is correctly considered.

We conclude from this analysis that experiment B is structurally different in its coupling of saturated plumes to the subcloud layer. It is more realistic than PP_a because (a) it contains a scale break in the plume number density, and (b) the rooting of the largest plumes to the subcloud layer is better. This clear link between the rooting of cumulus updrafts and the presence of the scale break is a new insight into the dynamics of continental shallow convection. The coupling of EDMF to BiOMi thus removed a compensating error in the PP_a configuration.
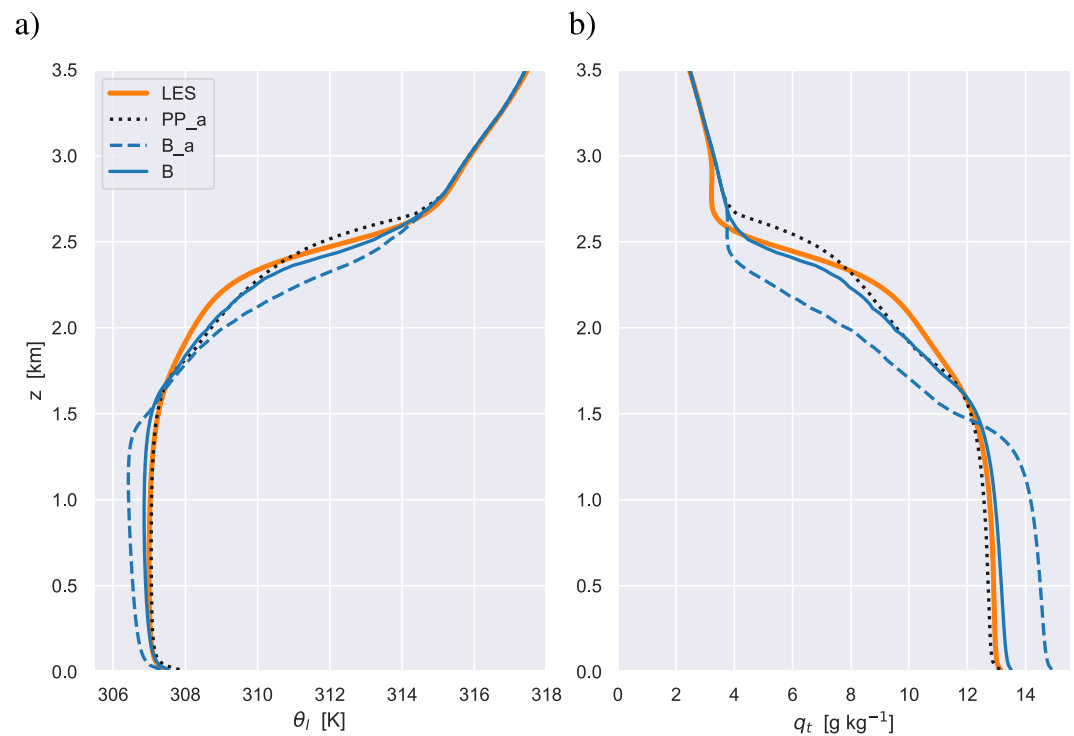
Figure 14. Same as Figure 9a but now showing $\overline{\theta}_l$ and $\overline{q}_t$ at 16:00 local time on 11 June 2016 for experiments PP_a (dotted black), B_a (dashed blue) and B (solid blue).
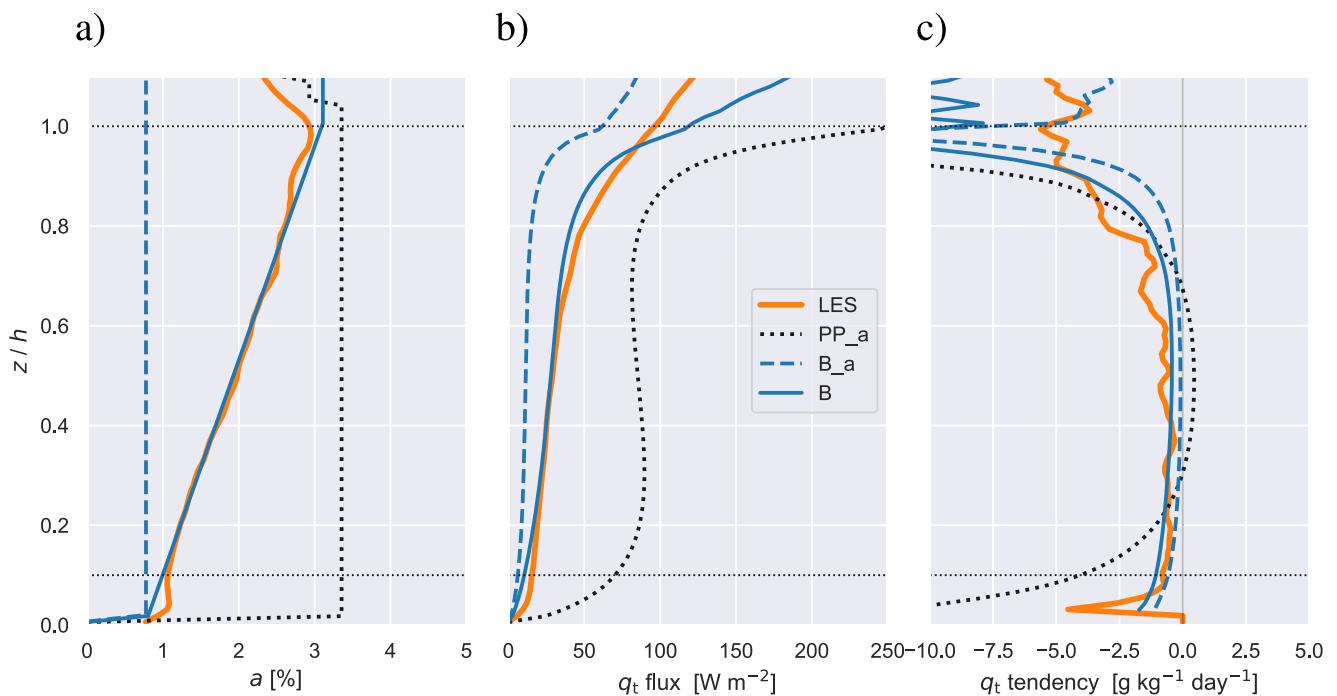
Figure 15. Profiles of average properties of the Super-Scale-break Size Segment (S^4), representing all plumes larger than the scale-break size. (a) Area fraction a, (b) convective q_t flux, and (b) the associated q_t tendencies calculated as the vertical flux convergence. Sampling time is 16:00 local time on 11 June 2016. LES is shown in orange, experiment PP_a in black, and B_a and B in dashed and solid blue, respectively. Height z is normalized by mixed layer depth (h).
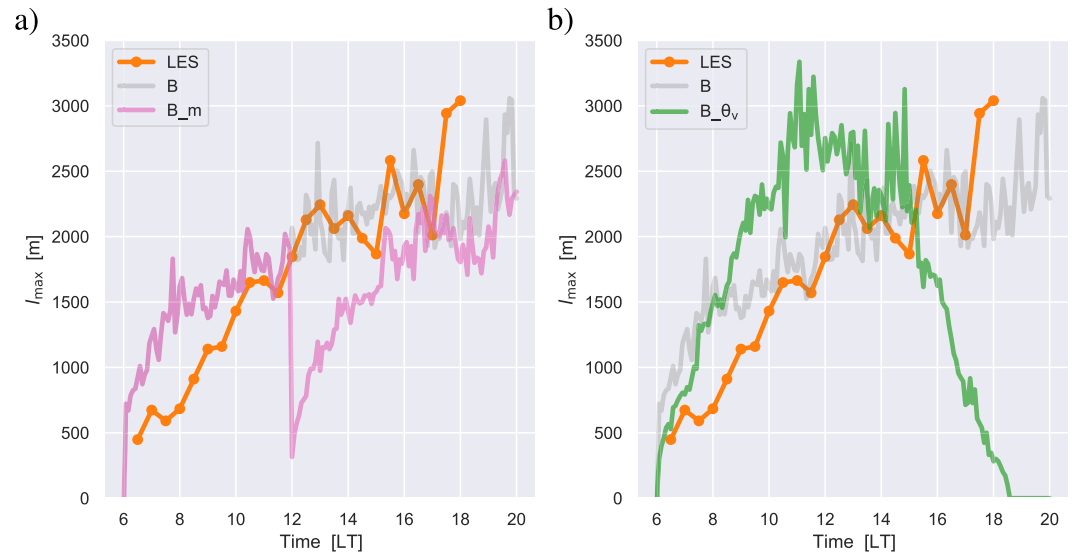
Figure 16. Time series of the largest cluster size l_{max} for (a) experiment B_m (pink) and (b) experiment B_θ_v (green). Experiment B and LES are also shown, for reference.

5.5. Two Sensitivity Experiments

In this section, two further experiments are discussed that are designed to provide further insight into the behavior of the framework.

The first experiment B_m is included to illustrate that the gradual scale growth on the microgrid can indeed be interpreted as convective memory. In this experiment, all thermals existing on the microgrid are randomly distributed at $t = 12$LT, while preserving total thermal number. The idea is to thus destroy any memory on the grid that is stored in the spatial clustering. Figure 16a shows that l_{max} drops immediately to about 300 m, and subsequently needs hours to recover. This shows that time is needed to grow the largest scales, and that their presence depends on what happened before (i.e., memory). Figure 17a shows that EDMF transport and clouds also collapse after the thermal redistribution. This indicates that the large clusters on the BiOMi microgrid that carry memory are needed to sustain boundary-layer deep transport in this framework.
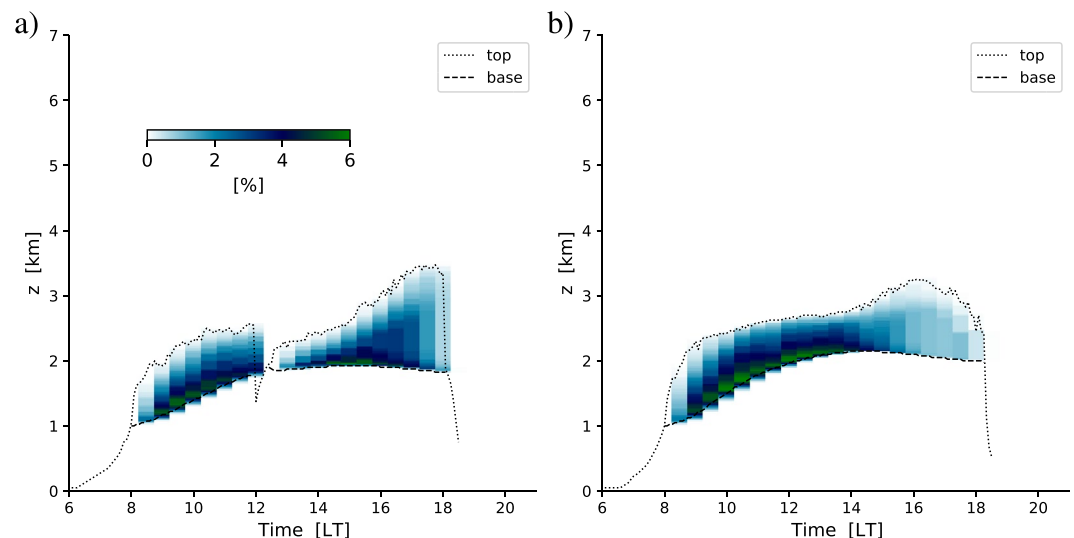
Figure 17. Time height plot of EDMF cloud fraction (a) experiment B_m and (b) experiment B_θ_v for 11 June 2016. The Lifting Condensation Level (black dashed) and maximum plume termination height (black dotted) are also shown, for reference.

The second experiment B_θ_v is designed to explore a candidate model for thermal births that is potentially more realistic, in that it follows a diurnal cycle instead of being constant. To this purpose, $\dot{B}$ is coupled to the surface buoyancy flux F_b^s,

$$F_b^s \;=\; \rho \; c_p \; \overline{w'\theta_v'}\Big|_s.$$

(10)

this energy flux is distributed over a number of convective thermals. Dividing the available flux by the typical energy contained in a single thermal, E_t yields the number of new thermals per unit time and area,

$$\dot{B} \;=\; \max\left[\frac{F_b^s}{E_t}, 0\right]$$

(11)

the thermal energy E_t can be thought of as including both potential energy (buoyancy) and kinetic energy (motion). Neglecting the latter for the moment, heating a near-surface thermal to be with a volume $V = 100^3$ m^3 by $\theta' = 1$ K at the prevailing air density yields a thermal energy of $E_t \sim 1e9$ J. Using this constant value results in total cluster areas $\mathcal{A}_c$ of comparable magnitude to experiment B. Near-surface instability thus acts as the slow driver in this setup, firing convective thermals when large and shutting down thermal births in (near-)stable conditions. The latter would be more in agreement with LES results on the decay of turbulence (Nieuwstadt & Brost, 1986). A consequence is that with this birth model, the total cluster area fraction A_c fed to EDMF is also no longer constant, and will follow a diurnal cycle. This should matter in particular toward the end of the day, when the surface buoyancy forcing reduces to zero.

Figure 16b shows that in experiment B_θ_v, the maximum cluster size $l_{\max}$ now also follows a diurnal cycle, introduced by the buoyancy flux through $\dot{B}$. Compared to the control experiment B, it spins up slower, but peaks larger, and then decreases to zero before sunset. The slower spin up is an improvement (i.e., more like LES), but the late afternoon decrease is in disagreement with LES, which maintains larger cluster sizes until 18 LT. The EDMF transport shows a substantial response to this reducing cluster size during the second half of the afternoon. The area of condensed transporting plumes in the cloud layer significantly reduces too soon during this second deepening phase, which is a direct consequence of the reducing cluster sizes on the microgrid. Comparison to the LES results in Figure 7a shows that this is unrealistic.

We conclude from these findings that (a) the pure diurnal cycle as a thermal birth model is also not adequate enough, and that (b) more research is needed to find out which birth model is the most successful in reproducing thermal clustering as diagnosed in LES. This might require moving toward a two-way coupling setup, and possibly a change in the rules of thermal interaction and their implementation. This is for now considered an open research question.

6. Discussion

The results show that the coupled BiOMi-ED(MF)^n framework reproduces the main vertical structure and diurnal evolution of the boundary layer to a satisfactory degree. That in itself is not trivial, because the coupling introduces quite a few degrees of freedom to the system of equations. Apparently, this does not cause instability; instead, smooth equilibration always occurs in response to slowly varying external forcings, yielding realistic transient boundary-layer states. Accordingly, this result provides proof of concept for frameworks of this kind.

We find that in this framework, diurnal scale growth does impact convective transport in a substantial way. This impact works through modulation of the number distribution of transporting objects, in response to their evolving spatial organization. A related insight is that plume vertical structure can no longer be ignored when coupling mass flux transport to a realistic cluster population that features a scale break in its number density. Adopting the differential rooting of plumes in the mixed layer as a function of size, as diagnosed in LES in the form of relation Equation 8, is needed to ensure that the group of largest plumes in the spectrum carry sufficient mass flux out of the mixed layer. Figure 18 schematically illustrates this concept. The deep rooting configuration combined with a scale break in the number density is supported by LES.

It is interesting to interpret this finding in the light of previous studies on cloud-subcloud coupling. While the existence of a general relationship between the distribution of cumulus clouds and their subcloud layer fluxes has long been known from pioneering early observational studies (LeMone & Pennell, 1976; Nicholls & Lemone, 1980),
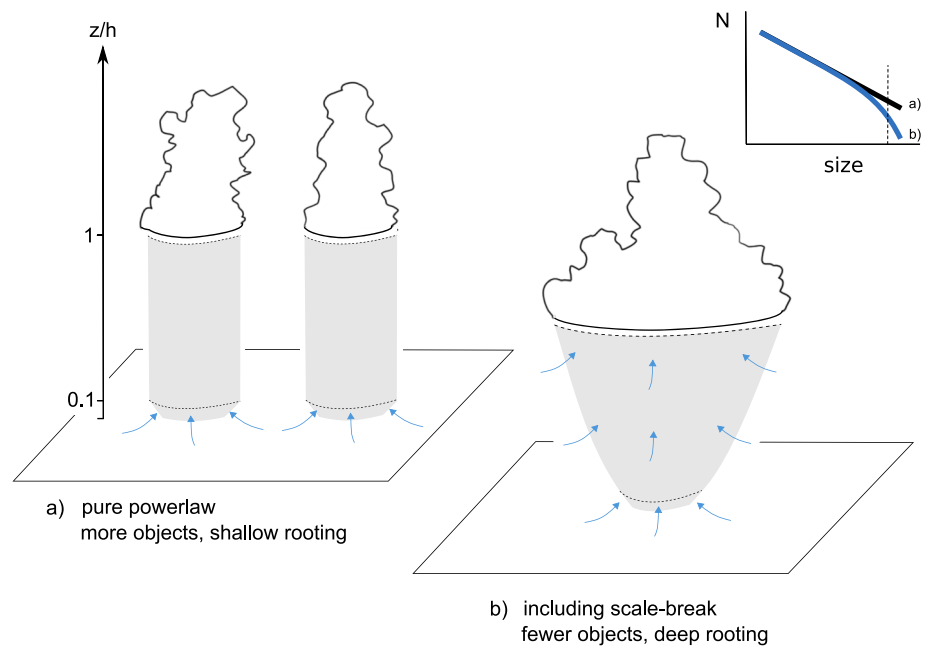
Figure 18. Schematic illustration of the two configurations of plume rooting as applied in the ED(MF)^n experiments in this study. (a) Shallow rooting with a pure powerlaw distribution of plume number. (b) Mixed-layer deep rooting for distributions including a scale break. Plume volume within the mixed layer is indicated by the gray shading. Height z is normalized by mixed-layer depth (h) Blue arrows indicate dynamic entrainment of mass into the plume. The associated two functional forms of the size distribution of plume number are shown in the inset. The deep rooting configuration (b) is supported by LES results.

our finding further nuances this relation by suggesting that rooting depends on plume size (see also Figure 5). This probably also plays a role in the transition from shallow to deep convection, where deep rooting is commonly observed (Mulholland et al., 2021).

We hypothesize the following physical-dynamical mechanism for explaining the link between plume rooting and the scale break. As soon as plumes saturate they also accelerate above their level of free convection, driven by latent heat release. Through continuity, the stronger vertical velocity has to imply an enhanced inflow of mass within their rooting layer, in this case the subcloud mixed layer. The boosted mass flux helps in overturning more instability in the domain, so that less remains for subsequent plumes. These strong plumes that reach saturation will occur less frequently as a result, which is reflected in the presence of the scale break. This hypothesis thus links the scale break directly to the phase change of water in coherent structures in the boundary layer, acting as a turbo charger for vertical mass transport. That the scale break size more or less coincides with the saturation point of ED(MF)^n plumes (see Figure 13b) would support this hypothesis.

Deep rooting is well known from studies of deep convection. For example, Williams and Stanfill (2002) and Mulholland et al. (2021) report that cumulus updraft width depends on height of the lifting condensation level, concluding that the width increases across the subcloud layer. Our analysis of shallow cumulus objects in Figure 5 suggests a similar dependence, in that low mixed-layer depths tend to be accompanied by small plume widths at $z = h$. However, the data also include some deep mixed layers with small updraft widths. These represent time-points late in the diurnal cycle, when the surface forcing of convection significantly weakens. Overall, we find that size dependence dominates over dependence on mixed-layer height. We speculate that these results are not in conflict with the deep convective studies, but instead could be explained by the following factors;

1. Differences in the type of convection (shallow vs. deep), including the presence of mesoscale structures such as cold pools;
2. Differences in sampling (here including both saturated and unsaturated plumes);
3. Differences in the case setup (composite vs. diurnal forcing).

More research is needed to gain insight, which could also further our understanding of the transition from shallow to deep convection.

The one-way coupling between BiOMi and ED(MF)^n used in this study in effect prescribes the scale break as used in convective transport. With the adopted settings, which were inspired by LES results (NG21), BiOMi does generate a plume distribution that evolves over time which also matches the evolution seen in LES. So this one-way setup has been sufficient for testing the scheme for the two shallow convection cases, and for providing proof of concept that the coupling in principle works. However, the growth rate of the cluster distribution, as well as its scaling behavior and cut-off point, likely depend on the settings in the rules of interaction. This also relates to the hypothesized mechanism for self-organizing criticality to occur under these rules, as suggested in Section 5.2 and which still needs to be tested. Similarly, it is important to calibrate the rules of interaction against independent data, ideally covering a broad range of atmospheric conditions.

In a more advanced setup, one could also think of adopting a two-way coupling, in which the work performed by the EDMF clusters affects the birth rate of thermals on the BiOMi microgrid. For example, one could introduce dependency on the potential energy available for convection. Adding this interaction might then allow abandoning the global constraint on the thermal birth rate, which is currently enforced through Rule 2. In this setup, the size distribution including the scale break could then evolve naturally from physical-dynamical processes. Implementing this two-way setup requires more research on the thermal birth rate and other statistics during diurnal cycles of convection over land. Previous studies have demonstrated that LES can well be used to this purpose (Hernandez-Deckers & Sherwood, 2016).

7. Conclusions

In this study, a spectral scheme for convective transport is coupled to a thermal population model on a horizontal microgrid. The goal is to thus enable impacts of spatial organization on parameterized convective transport. The BiOMi-ED(MF)^n framework is tested for two observed diurnal cycles of shallow convection at the ARM SGP site. A main outcome is that the results provide proof of concept for decentralized frameworks of this kind. It reproduces realistic diurnal cycles for 2 days that differ considerably in terms of cloud properties, without any artificial instability as a result of the coupling. Another key result it that characteristics of self-organizing criticality are reproduced, including (a) powerlaw scaling below a scale break in the number density and (b) gradual scale growth and spatial organization during the day. Exploring the framework, we find that convective organization for these kind of shallow cumulus cloud fields can significantly impact vertical transport through its control over the number density of convective objects. Targeted sensitivity tests suggest a tight link between the presence of a scale break and the way plumes root in the subcloud layer. Adopting differential plume rooting as a function of size is required for coupling convective transport to a realistic population of convective objects.

While this study provides proof of concept, the results also suggest that more research is needed into the birth of thermals in convective layers. BiOMi-ED(MF)^n also still needs to be thoroughly calibrated and evaluated to test general applicability. This could be achieved by significantly expanding the number of cases, for example, by using the full library of LASSO shallow cumulus days at SGP. Another important step is to include new rules of interaction to capture impacts of precipitation and wind shear on spatial organization in cumulus cloud populations, which are known to be significant. Objective calibration of constants of proportionality against large data sets is ongoing work by the authors, including the use of machine learning algorithms.

BiOMi-ED(MF)^n could function as a subgrid convection scheme in an operational weather or climate model. A first step toward this goal could be to simply add columns to the DALES macrogrid, and (re)activate all terms in the governing equations for the resolved flow. This way, the mean state across all columns can interact again (Brast et al., 2018). In this Multi Column Model setup (Hwong et al., 2022), experiments can be conducted for larger domains in which feedbacks between subgrid convection and the larger-scale circulation can take place naturally. Another advantage is that the complexity of the resolved flow is still much lower compared to a realistic GCM, which might help in gaining a better understanding of the newly introduced feedbacks.

The BiOMi model as applied to populations of convective thermals could be combined with other recent EDMF (Cohen et al., 2020; Lopez-Gomez et al., 2020) or two-fluid approaches (Shipley et al., 2022; Thuburn et al., 2018; Weller & McIntyre, 2019), for example, by providing a boundary condition in the form of a time-varying vertically projected updraft area fraction. The horizontal microgrid is also convenient for introducing gray zone effects

(Honnert et al., 2020; Plant & Craig, 2008; Wyngaard, 2004), in that it automatically captures the subsampling of a convective population at too small macrogrid cell sizes. A further interesting opportunity would be to connect microgrids between neighboring macrogrid columns, which in principle would allow unimpeded cluster growth on the interconnected microgrids. This might address earlier reported problems in the gray zone, in the shape of artificial circulations on the macrogrid close to the grid scale (Sakradzija et al., 2016). Another opportunity created by the horizontal microgrid is to connect thermal birth to small-scale surface heterogeneity, which could thus impact convective triggering. Pursuing these ideas is a future research plan.

Data Availability Statement

Data were obtained from the Atmospheric Radiation Measurement (ARM) Program sponsored by the U.S. Department of Energy, Office of Science, Office of Biological and Environmental Research, Climate and Environmental Sciences Division. LASSO data were used from the U.S. Department of Energy's ARM Climate Research Facility. Data used in the figures in this manuscript are available at https://doi.org/10.5281/zenodo.6044338. The Binomials On Microgrids code repository is available on Github at https://github.com/pgriewank/BiOMi.

References

Ahmed, F., & Neelin, J. D. (2019). Explaining scales and statistics of tropical precipitation clusters with a stochastic model. *Journal of the Atmospheric Sciences*, *76*(10), 3063–3087. https://doi.org/10.1175/JAS-D-18-0368.1

Arakawa, A. (2004). The cumulus parameterization problem: Past, present, and future. *Journal of Climate*, *17*(13), 2493–2525. https://doi.org/10.1175/1520-0442(2004)017<2493:RATCPP>2.0.CO;2

Bak, P., Tang, C., & Wiesenfeld, K. (1987). Self-organized criticality: An explanation of the 1/f noise. *Physical Review Letters*, *59*(4), 381–384. https://doi.org/10.1103/PhysRevLett.59.381

Bengtsson, L., Dias, J., Tulich, S., Gehne, M., & Bao, J.-W. (2021). A stochastic parameterization of organized tropical convection using cellular automata for global forecasts in NOAA's unified forecast system. *Journal of Advances in Modeling Earth Systems*, *13*(1), e2020MS002260. https://doi.org/10.1029/2020MS002260

Böing, S. J. (2016). An object-based model for convective cold pool dynamics. *Mathematics of Climate and Weather Forecasting*, *2*(1). https://doi.org/10.1515/mcwf-2016-0003

Bony, S., Stevens, B., Ament, F., Bigorre, S., Chazette, P., Crewell, S., et al. (2017). EUREC4A: A field campaign to elucidate the couplings between clouds, convection and circulation. *Surveys in Geophysics*, *38*(6), 1529–1568. https://doi.org/10.1007/s10712-017-9428-0

Brast, M., Schemann, V., & Neggers, R. A. J. (2018). Investigating the scale adaptivity of a size-filtered mass flux parameterization in the gray zone of shallow cumulus convection. *Journal of the Atmospheric Sciences*, *75*(4), 1195–1214. https://doi.org/10.1175/JAS-D-17-0231.1

Bretherton, C. S., Blossey, P. N., & Khairoutdinov, M. (2005). An energy-balance analysis of deep convective self-aggregation above uniform SST. *Journal of the Atmospheric Sciences*, *62*(12), 4273–4292. https://doi.org/10.1175/JAS3614.1

Bretherton, C. S., & Smolarkiewicz, P. K. (1989). Gravity waves, compensating subsidence and detrainment around cumulus clouds. *Journal of the Atmospheric Sciences*, *46*(6), 740–759. https://doi.org/10.1175/1520-0469(1989)046<0740:GWCSAD>2.0.CO;2

Brient, F., Couvreux, F., Villefranque, N., Rio, C., & Honnert, R. (2019). Object-oriented identification of coherent structures in large eddy simulations: Importance of downdrafts in stratocumulus. *Geophysical Research Letters*, *46*(5), 2854–2864. https://doi.org/10.1029/2018GL081499

Brown, A. R., Cederwall, R. T., Chlond, A., Duynkerke, P. G., Golaz, J.-C., Khairoutdinov, M., et al. (2002). Large-eddy simulation of the diurnal cycle of shallow cumulus convection over land. *Quarterly Journal of the Royal Meteorological Society*, *128*(582), 1075–1094. https://doi.org/10.1256/003590002320373210

Chen, J., Hagos, S., Xiao, H., Fast, J. D., & Feng, Z. (2020). Characterization of surface heterogeneity-induced convection using cluster analysis. *Journal of Geophysical Research: Atmospheres*, *125*(20), e2020JD032550. https://doi.org/10.1029/2020JD032550

Clark, P. A., Halliwell, C. E., & Flack, D. L. A. (2021). A physically based stochastic boundary layer perturbation scheme. Part I: Formulation and evaluation in a convection-permitting model. *Journal of the Atmospheric Sciences*, *78*(3), 727–746. https://doi.org/10.1175/JAS-D-19-0291.1

Cohen, Y., Lopez-Gomez, I., Jaruga, A., He, J., Kaul, C. M., & Schneider, T. (2020). Unified entrainment and detrainment closures for extended eddy-diffusivity mass-flux schemes. *Journal of Advances in Modeling Earth Systems*, *12*(9), e2020MS002162. https://doi.org/10.1029/2020MS002162

Couvreux, F., Hourdin, F., & Rio, C. (2009). Resolved versus parametrized boundary-layer plumes. Part I: A parametrization-oriented conditional sampling in large-eddy simulations. *Boundary-Layer Meteorology*, *134*(3), 441–458. https://doi.org/10.1007/s10546-009-9456-5

de Roode, S. R., Siebesma, A. P., Jonker, H. J. J., & de Voogd, Y. (2012). Parameterization of the vertical velocity equation for shallow cumulus clouds. *Monthly Weather Review*, *140*(8), 2424–2436. https://doi.org/10.1175/MWR-D-11-00277.1

de Rooy, W. C., Bechtold, P., Fröhlich, K., Hohenegger, C., Jonker, H., Mironov, D., et al. (2013). Entrainment and detrainment in cumulus convection: An overview. *Quarterly Journal of the Royal Meteorological Society*, *139*(670), 1–19. https://doi.org/10.1002/qj.1959

Dorrestijn, J., Crommelin, D. T., Biello, J. A., & Böing, S. J. (2013). A data-driven multi-cloud model for stochastic parametrization of deep convection. *Philosophical Transactions of the Royal Society A: Mathematical, Physical & Engineering Sciences*, *371*(1991), 20120374. https://doi.org/10.1098/rsta.2012.0374

Drueke, S., Kirshbaum, D. J., & Kollias, P. (2021). Environmental sensitivities of shallow-cumulus dilution—Part 2: Vertical wind profile. *Atmospheric Chemistry and Physics*, *21*(18), 14039–14058. https://doi.org/10.5194/acp-21-14039-2021

Fast, J. D., Berg, L. K., Alexander, L., Bell, D., D'Ambro, E., Hubbe, J., et al. (2019). Overview of the hi-scale field campaign: A new perspective on shallow convective clouds. *Bulletin of the American Meteorological Society*, *100*(5), 821–840. https://doi.org/10.1175/BAMS-D-18-0030.1

Gentine, P., Holtslag, A. A. M., D'Andrea, F., & Ek, M. (2013). Surface and atmospheric controls on the onset of moist convection over land. *Journal of Hydrometeorology*, *14*(5), 1443–1462. https://doi.org/10.1175/JHM-D-12-0137.1

Grabowski, W. W., Bechtold, P., Cheng, A., Forbes, R., Halliwell, C., Khairoutdinov, M., et al. (2006). Daytime convective development over land: A model intercomparison based on LBA observations. *Quarterly Journal of the Royal Meteorological Society*, *132*(615), 317–344. https://doi.org/10.1256/qj.04.147

Griewank, P. J., Heus, T., & Neggers, R. (2021). Size-dependence of surface-rooted three-dimensional convective objects in continental shallow cumulus simulations. *Earth and Space Science Open Archive*, *37*. https://doi.org/10.1002/essoar.10507029.1

Gustafson, W. I., Vogelmann, A. M., Cheng, X., Endo, S., Krishna, B., Li, Z., et al. (2017a). Atmospheric Radiation Measurement (ARM) Research Facility. September 2017. LASSO Alpha 2 Data Bundles. 36° 36′ 18.0′′ N, 97° 29′ 6.0′′ W: Southern Great Plains Central Facility (C1). https://doi.org/10.5439/1342961

Gustafson, W. I., Vogelmann, A. M., Cheng, X., Endo, S., Krishna, B., Li, Z., et al. (2017b). Description of the lasso alpha 2 release. https://doi.org/10.2172/1376727

Gustafson, W. I., Vogelmann, A. M., Li, Z., Cheng, X., Dumas, K. K., Endo, S., et al. (2020). The large-eddy simulation (LES) atmospheric radiation measurement (ARM) symbiotic simulation and observation (LASSO) activity for continental shallow convection. *Bulletin of the American Meteorological Society*, *101*(4), E462–E479. https://doi.org/10.1175/BAMS-D-19-0065.1

Haerter, J. O., Böing, S. J., Henneberg, O., & Nissen, S. B. (2019). Circling in on convective organization. *Geophysical Research Letters*, *46*(12), 7024–7034. https://doi.org/10.1029/2019GL082092

Hernandez-Deckers, D., & Sherwood, S. C. (2016). A numerical investigation of cumulus thermals. *Journal of the Atmospheric Sciences*, *73*(10), 4117–4136. https://doi.org/10.1175/JAS-D-15-0385.1

Heus, T., Heerwaarden, C. C., Jonker, H. J. J., Siebesma, A. P., Axelsen, S., van den Dries, K., et al. (2010). Formulation of the Dutch atmospheric large-eddy simulation (DALES) and overview of its applications. *Geoscientific Model Development*, *3*(2), 415–444. https://doi.org/10.5194/gmd-3-415-2010

Hirt, M., Rasp, S., Blahak, U., & Craig, G. C. (2019). Stochastic parameterization of processes leading to convective initiation in kilometer-scale models. *Monthly Weather Review*, *147*(11), 3917–3934. https://doi.org/10.1175/MWR-D-19-0060.1

Honnert, R., Efstathiou, G. A., Beare, R. J., Ito, J., Lock, A., Neggers, R., et al. (2020). The atmospheric boundary layer and the "gray zone" of turbulence: A critical review. *Journal of Geophysical Research: Atmospheres*, *125*(13), e2019JD030317. https://doi.org/10.1029/2019JD030317

Hottovy, S., & Stechmann, S. N. (2015). A spatiotemporal stochastic model for tropical precipitation and water vapor dynamics. *Journal of the Atmospheric Sciences*, *72*(12), 4721–4738. https://doi.org/10.1175/JAS-D-15-0119.1

Houghton, H. G., & Cramer, H. E. (1951). A theory of entrainment in convective currents. *Journal of the Atmospheric Sciences*, *8*(2), 95–102. https://doi.org/10.1175/1520-0469(1951)008<0095:ATOEIC>2.0.CO;2

Hwong, Y.-L., Sherwood, S. C., & Fuchs, D. (2022). Can we use 1D models to predict 3D model response to forcing in an idealized framework? *Journal of Advances in Modeling Earth Systems*, *14*(4), e2021MS002785. https://doi.org/10.1029/2021MS002785

Jansson, F., van den Oord, G., Pelupessy, I., Grönqvist, J. H., Siebesma, A. P., & Crommelin, D. (2019). Regional superparameterization in a global circulation model using large eddy simulations. *Journal of Advances in Modeling Earth Systems*, *11*(9), 2958–2979. https://doi.org/10.1029/2018MS001600

Jensen, M., Giangrande, S., Fairless, T., & Zhou, A. (nd). Interpolated sonde (interpolatedsonde). https://doi.org/10.5439/1095316

Khouider, B., Biello, J., & Majda, A. J. (2010). A stochastic multicloud model for tropical convection. *Communications in Mathematical Sciences*, *8*(1), 187–216. https://doi.org/10.4310/cms.2010.v8.n1.a10

Klingebiel, M., Konow, H., & Stevens, B. (2021). Measuring shallow convective mass flux profiles in the trade wind region. *Journal of the Atmospheric Sciences*, *78*(10), 3205–3214. https://doi.org/10.1175/JAS-D-20-0347.1

Kober, K., & Craig, G. C. (2016). Physically based stochastic perturbations (PSP) in the boundary layer to represent uncertainty in convective initiation. *Journal of the Atmospheric Sciences*, *73*(7), 2893–2911. https://doi.org/10.1175/JAS-D-15-0144.1

LeMone, M. A., & Pennell, W. T. (1976). The relationship of trade wind cumulus distribution to subcloud layer fluxes and structure. *Monthly Weather Review*, *104*(5), 524–539. https://doi.org/10.1175/1520-0493(1976)104<0524:TROTWC>2.0.CO;2

Lenschow, D., & Stephens, P. (1980). The role of thermals in the convective boundary layer. *Boundary-Layer Meteorology*, *19*(4), 509–532. https://doi.org/10.1007/BF00122351

Lopez-Gomez, I., Cohen, Y., He, J., Jaruga, A., & Schneider, T. (2020). A generalized mixing length closure for eddy-diffusivity mass-flux schemes of turbulence and convection. *Journal of Advances in Modeling Earth Systems*, *12*(11), e2020MS002161. https://doi.org/10.1029/2020MS002161

Mather, J. H., & Voyles, J. W. (2013). The arm climate research facility: A review of structure and capabilities. *Bulletin of the American Meteorological Society*, *94*(3), 377–392. https://doi.org/10.1175/BAMS-D-11-00218.1

Morrison, H., & Peters, J. M. (2018). Theoretical expressions for the ascent rate of moist deep convective thermals. *Journal of the Atmospheric Sciences*, *75*(5), 1699–1719. https://doi.org/10.1175/JAS-D-17-0295.1

Mulholland, J. P., Peters, J. M., & Morrison, H. (2021). How does lcl height influence deep convective updraft width? *Geophysical Research Letters*, *48*(13), e2021GL093316. https://doi.org/10.1029/2021GL093316

Muller, C. J., & Held, I. M. (2012). Detailed investigation of the self-aggregation of convection in cloud-resolving simulations. *Journal of the Atmospheric Sciences*, *69*(8), 2551–2565. https://doi.org/10.1175/JAS-D-11-0257.1

Neggers, R. A. J. (2015). Exploring bin-macrophysics models for moist convective transport and clouds. *Journal of Advances in Modeling Earth Systems*, *7*(4), 2079–2104. https://doi.org/10.1002/2015MS000502

Neggers, R. A. J., & Griewank, P. J. (2021). A binomial stochastic framework for efficiently modeling discrete statistics of convective populations. *Journal of Advances in Modeling Earth Systems*, *13*(3), e2020MS002229. https://doi.org/10.1029/2020MS002229

Neggers, R. A. J., Griewank, P. J., & Heus, T. (2019). Power-law scaling in the internal variability of cumulus cloud size distributions due to subsampling and spatial organization. *Journal of the Atmospheric Sciences*, *76*(6), 1489–1503. https://doi.org/10.1175/JAS-D-18-0194.1

Neggers, R. A. J., Jonker, H. J. J., & Siebesma, A. P. (2003). Size statistics of cumulus cloud populations in large-eddy simulations. *Journal of the Atmospheric Sciences*, *60*(8), 1060–1074. https://doi.org/10.1175/1520-0469(2003)60<1060:SSOCCP>2.0.CO;2

Neggers, R. A. J., Siebesma, A. P., & Jonker, H. J. J. (2002). A multiparcel model for shallow cumulus convection. *Journal of the Atmospheric Sciences*, *59*(10), 1655–1668. https://doi.org/10.1175/1520-0469(2002)059<1655:AMMFSC>2.0.CO;2

Nicholls, S., & Lemone, M. A. (1980). The fair weather boundary layer in gate: The relationship of subcloud fluxes and structure to the distribution and enhancement of cumulus clouds. *Journal of the Atmospheric Sciences*, *37*(9), 2051–2067. https://doi.org/10.1175/1520-0469(1980)037<2051:TFWBLI>2.0.CO;2

Nieuwstadt, F. T. M., & Brost, R. A. (1986). The decay of convective turbulence. *Journal of the Atmospheric Sciences*, *43*(6), 532–546. https://doi.org/10.1175/1520-0469(1986)043<0532:TDOCT>2.0.CO;2

Peters, J. M., Nowotarski, C. J., & Mullendore, G. L. (2020). Are supercells resistant to entrainment because of their rotation? *Journal of the Atmospheric Sciences*, *77*(4), 1475–1495. https://doi.org/10.1175/JAS-D-19-0316.1

Plant, R. S., & Craig, G. C. (2008). A stochastic parameterization for deep convection based on equilibrium statistics. *Journal of the Atmospheric Sciences*, *65*(1), 87–105. https://doi.org/10.1175/2007JAS2263.1

Quinn, K. M., & Neelin, J. D. (2017). Distributions of tropical precipitation cluster power and their changes under global warming. Part I: Observational baseline and comparison to a high-resolution atmospheric model. *Journal of Climate*, *30*(20), 8033–8044. https://doi.org/10.1175/JCLI-D-16-0683.1

Randall, D., Khairoutdinov, M., Arakawa, A., & Grabowski, W. (2003). Breaking the cloud parameterization deadlock. *Bulletin of the American Meteorological Society*, *84*(11), 1547–1564. https://doi.org/10.1175/BAMS-84-11-1547

Romps, D. M., Öktem, R., Endo, S., & Vogelmann, A. M. (2021). On the life cycle of a shallow cumulus cloud: Is it a bubble or plume, active or forced? *Journal of the Atmospheric Sciences*, *78*(9), 2823–2833. https://doi.org/10.1175/JAS-D-20-0361.1

Sakradzija, M., Seifert, A., & Dipankar, A. (2016). A stochastic scale-aware parameterization of shallow cumulus convection across the convective gray zone. *Journal of Advances in Modeling Earth Systems*, *8*(2), 786–812. https://doi.org/10.1002/2016MS000634

Scorer, R. S., & Ludlam, F. H. (1953). Bubble theory of penetrative convection. *Quarterly Journal of the Royal Meteorological Society*, *79*(339), 94–103. https://doi.org/10.1002/qj.49707933908

Sherwood, S. C., Bony, S., & Dufresne, J. (2014). Spread in model climate sensitivity traced to atmospheric convective mixing. *Nature*, *505*(7481), 37–42. https://doi.org/10.1038/nature12829

Shipley, D., Weller, H., Clark, P. A., & McIntyre, W. A. (2022). Two-fluid single-column modelling of Rayleigh–Bénard convection as a step towards multi-fluid modelling of atmospheric convection. *Quarterly Journal of the Royal Meteorological Society*, *148*(742), 351–377. https://doi.org/10.1002/qj.4209

Siebesma, A. P., Soares, P. M. M., & Teixeira, J. (2007). A combined eddy-diffusivity mass-flux approach for the convective boundary layer. *Journal of the Atmospheric Sciences*, *64*(4), 1230–1248. https://doi.org/10.1175/JAS3888.1

Simpson, J., & Wiggert, V. (1969). Models of precipitating cumulus towers. *Monthly Weather Review*, *97*(7), 471–489. https://doi.org/10.1175/1520-0493(1969)097<0471:MOPCT>2.3.CO;2

Stevens, B., Bony, S., Brogniez, H., Hentgen, L., Hohenegger, C., Kiemle, C., et al. (2020). Sugar, gravel, fish and flowers: Mesoscale cloud patterns in the trade winds. *Quarterly Journal of the Royal Meteorological Society*, *146*(726), 141–152. https://doi.org/10.1002/qj.3662

Stokes, G. M., & Schwartz, S. E. (1994). The atmospheric radiation measurement (arm) program: Programmatic background and design of the cloud and radiation test bed. *Bulletin of the American Meteorological Society*, *75*(7), 1201–1222. https://doi.org/10.1175/1520-0477(1994)075<1201:TARMPP>2.0.CO;2

Thuburn, J., Weller, H., Vallis, G. K., Beare, R. J., & Whitall, M. (2018). A framework for convection and boundary layer parameterization derived from conditional filtering. *Journal of the Atmospheric Sciences*, *75*(3), 965–981. https://doi.org/10.1175/JAS-D-17-0130.1

Tiedtke, M. (1989). A comprehensive mass flux scheme for cumulus parameterization in large-scale models. *Monthly Weather Review*, *117*(8), 1779–1800. https://doi.org/10.1175/1520-0493(1989)117<1779:ACMFSF>2.0.CO;2

Tompkins, A. M., & Semie, A. G. (2017). Organization of tropical convection in low vertical wind shears: Role of updraft entrainment. *Journal of Advances in Modeling Earth Systems*, *9*(2), 1046–1068. https://doi.org/10.1002/2016MS000802

Turner, J. S. (1962). The "starting plume" in neutral surroundings. *Journal of Fluid Mechanics*, *13*(3), 356–368. https://doi.org/10.1017/S0022112062000762

van Heerwaarden, C. C., van Stratum, B. J. H., Heus, T., Gibbs, J. A., Fedorovich, E., & Mellado, J. P. (2017). Microhh 1.0: A computational fluid dynamics code for direct numerical simulation and large-eddy simulation of atmospheric boundary layer flows. *Geoscientific Model Development*, *10*(8), 3145–3165. https://doi.org/10.5194/gmd-10-3145-2017

van Laar, T. W., Schemann, V., & Neggers, R. A. J. (2019). Investigating the diurnal evolution of the cloud size distribution of continental cumulus convection using multiday les. *Journal of the Atmospheric Sciences*, *76*(3), 729–747. https://doi.org/10.1175/JAS-D-18-0084.1

Varble, A., Nesbitt, S. W., Salio, P., Hardin, J. C., Bharadwaj, N., Borque, P., et al. (2021). Utilizing a storm-generating hotspot to study convective cloud transitions: The cacti experiment. *Bulletin of the American Meteorological Society*, *102*(8), E1597–E1620. https://doi.org/10.1175/BAMS-D-20-0030.1

Varble, A., Zipser, E. J., Fridlind, A. M., Zhu, P., Ackerman, A. S., Chaboureau, J.-P., et al. (2014). Evaluation of cloud-resolving and limited area model intercomparison simulations using twp-ice observations: 1. Deep convective updraft properties. *Journal of Geophysical Research: Atmospheres*, *119*(24), 13891–13918. https://doi.org/10.1002/2013JD021371

Vogel, R., Nuijens, L., & Stevens, B. (2016). The role of precipitation and spatial organization in the response of trade-wind clouds to warming. *Journal of Advances in Modeling Earth Systems*, *8*(2), 843–862. https://doi.org/10.1002/2015MS000568

Weller, H., & McIntyre, W. A. (2019). Numerical solution of the conditionally averaged equations for representing net mass flux due to convection. *Quarterly Journal of the Royal Meteorological Society*, *145*(721), 1337–1353. https://doi.org/10.1002/qj.3490

Williams, E., & Stanfill, S. (2002). The physical origin of the land–ocean contrast in lightning activity. *Comptes Rendus Physique*, *3*(10), 1277–1292. https://doi.org/10.1016/S1631-0705(02)01407-X

Wing, A. A., Stauffer, C. L., Becker, T., Reed, K. A., Ahn, M.-S., Arnold, N. P., et al. (2020). Clouds and convective self-aggregation in a multi-model ensemble of radiative-convective equilibrium simulations. *Journal of Advances in Modeling Earth Systems*, *12*(9), e2020MS002138. https://doi.org/10.1029/2020MS002138

Wyngaard, J. C. (2004). Toward numerical modeling in the "Terra Incognita". *Journal of the Atmospheric Sciences*, *61*(14), 1816–1826. https://doi.org/10.1175/1520-0469(2004)061<1816:TNMITT>2.0.CO;2

Zhang, M., Bretherton, C. S., Blossey, P. N., Austin, P. H., Bacmeister, J. T., Bony, S., et al. (2013). CGILS: Results from the first phase of an international project to understand the physical mechanisms of low cloud feedbacks in single column models. *Journal of Advances in Modeling Earth Systems*, *5*(4), 826–842. https://doi.org/10.1002/2013MS000246

Zhang, Y., & Klein, S. (2010). Mechanisms affecting the transition from shallow to deep convection over land: Inferences from observations of the diurnal cycle collected at the arm southern Great Plains site. *Journal of the Atmospheric Sciences*, *67*(9), 2943–2959. https://doi.org/10.1175/2010JAS3366.1